

Observability Analysis and Keyframe-Based Filtering for Visual Inertial Odometry with Full Self-Calibration

Jianzhu Huai¹, *Member, IEEE*, Yukai Lin², Yuan Zhuang^{1†}, *Member, IEEE*
Charles Toth³, *Senior Member, IEEE*, and Dong Chen¹, *Member, IEEE*

Abstract—Camera-IMU (Inertial Measurement Unit) sensor fusion has been extensively studied in recent decades. Numerous observability analysis and fusion schemes for motion estimation with self-calibration have been presented. However, it has been uncertain whether both camera and IMU intrinsic parameters are observable under general motion. To answer this question, we first prove that for a global shutter camera-IMU system, all intrinsic and extrinsic parameters are observable with an unknown landmark. Given this, time offset and readout time of a rolling shutter (RS) camera also prove to be observable. Next, to validate this analysis and to solve the drift issue of a structureless filter during standstills, we develop a Keyframe-based Sliding Window Filter (KSWF) for odometry and self-calibration, which works with a monocular RS camera or stereo RS cameras. Though the keyframe concept is widely used in vision-based sensor fusion, to our knowledge, KSWF is the first of its kind to support self-calibration. Our simulation and real data tests validated that it is possible to fully calibrate the camera-IMU system using observations of opportunistic landmarks under diverse motion. Real data tests confirmed previous allusions that keeping landmarks in the state vector can remedy the drift in standstill, and showed that the keyframe-based scheme is an alternative cure.

Index Terms—keyframe-based sliding window filter, observability analysis, rolling shutter, visual inertial odometry, self-calibration

I. INTRODUCTION

VISUAL Inertial Odometry (VIO) estimates the motion of an agent using data captured by the rigidly mounted cameras and Inertial Measurement Units (IMUs). With great potential for augmented reality and robotics, many VIO methods have been developed and deployed on smartphones [1], unmanned aerial vehicles [2], floor-cleaning robots [3], and delivery robots [4]. However, these methods still have many weaknesses related to dynamic scenes [5], unstable initialization [6], coarse sensor calibration [7], and degenerate motion [8], to name a few. In an effort to build low-cost and robust VIO systems, this paper looks into the last two problems.

For most VIO methods, proper camera-IMU system calibration is ineluctable in achieving accurate motion estimation

[7] and stable initialization [6]. But millions of consumer products, *e.g.*, smartphones, often have low-cost sensors that are inaccurately calibrated. For such sensor systems, real-time self-calibration along with motion estimation has become a viable option, motivated by the ensuing benefits. First, additional computation for self-calibration is marginal and usually improves motion estimation [9], [10]. Second, this capability can be disabled online to save power if need be. Third, self-calibration also comes in handy when dealing with legacy data captured without premeditated calibration. Thus, current VIO methods usually have some ability to calibrate the sensor system, especially the IMU biases and camera extrinsic parameters, *e.g.*, [11], [12]. One question underlying self-calibration is whether the calibration parameters are observable. Several works have analyzed observability of camera extrinsics [13], camera intrinsics [14], and IMU intrinsics [15]. There is empirical evidence [9], [16] that the camera-related parameters and IMU intrinsic parameters could be jointly estimated in VIO, but there lacks a formal proof for this full self-calibration.

Ideally, a VIO method should exhibit little drift when the system goes through degenerate motion, *e.g.*, standstill. Although filtering-based VIO systems have been taking the lead in research and commercial products [1], [17] because of its efficiency among the existing geometrical approaches, quite a few of them suffer from drift during degenerate motion [18]. One influential strand of filters stems from the multi-state constraint Kalman filter (MSCKF) [19]. In contrast to the EKF style filters which keep the latest motion variables and a set of landmarks in the state, *e.g.*, [20], [12], MSCKFs [21], [10] keep in the state vector a sliding window of motion variables associated with images but not landmarks (hence structureless or memoryless). Despite the efficiency brought about by the disposal of landmarks, existing structureless filters for monocular VIO are prone to dramatic drift under degenerate motion, *e.g.* hovering or standstill [18]. Several attempts have been made to address this issue. A state management strategy based on the last-in-first-out rule was presented in [8], but it requires detecting hovering. OpenVINS [10] deals with standstills by using zero velocity update (ZUPT) which again requires motion detection heuristics.

This paper tries to address the above two challenges to VIO, inaccurate sensor calibration and degenerate motion. First, we advocate calibrating the visual inertial system by fully accounting for relevant sensor parameters, and support

¹J. Huai, Y. Zhuang, D. Chen are with the State Key Laboratory of Information Engineering in Surveying, Mapping, and Remote Sensing (LIES-MARS), Wuhan University, 129 Luoyu Road, Wuhan, Hubei, 430079, China. Homepage of J. Huai: <https://www.jianzhuohuai.com/>.

²Y. Lin is with Huawei, Shanghai, China.

³Charles Toth is with the Department of Civil, Environmental, and Geodetic Engineering, The Ohio State University, Columbus, OH 43210, USA.

[†]Corresponding author, yuan.zhuang@whu.edu.cn.

its feasibility by a thorough observability analysis. Second, we propose a Keyframe-based Sliding Window Filter (KSWF), leveraging keyframes to handle degenerate motion.

Specifically, first, we develop the observability analysis of a VIO system that self-calibrates camera intrinsic and extrinsic parameters and IMU intrinsics in an unknown environment, with the Observability Rank Condition (ORC) [22], [23] of Lie derivatives. Under general motion, these parameters prove to be observable. Conditioned on this, we further prove that the camera time offset and rolling shutter (RS) readout time are also able to be estimated. To our knowledge, observability analysis for the full calibration has not been done before.

Then, the KSWF with self-calibration is presented for setups consisting of an IMU and one or two cameras. Its frontend takes as input from the camera rig a sequence of frames or roughly synced frame pairs (called frame bundles for generality), associates keypoints between frames, and selects keyframe bundles based on view overlaps. The backend filter keeps in the state vector a sliding window of motion state variables which will be opportunely marginalized depending on whether they are associated with keyframe bundles, and opportunistic landmarks. As keyframes typically do not change when the platform goes through degenerate motion, the keyframe-based scheme is resilient to standstill and hovering. Granted that KSWF has similarities with recent VIO methods, it is unique in several ways. For example, compared to the original MSCKF [19], KSWF is equipped with support for RS effect and stereo camera setups, full self-calibration, keyframe-based feature matching, and keyframe-based state management.

Lastly, in simulation and real world tests with KSWF, we validate that the camera and IMU calibration parameters are observable and self-calibration improves motion estimation under general motion, and that the drift of existing monocular structureless filters in degenerate motion can be mitigated by the keyframe-based scheme.

The next section reviews recent developments on VIO from the aspects of observability analysis and real-time motion estimation with degenerate motion and distinguishes our study from related ones. Section III describes the proposed KSWF including measurement models, state vector, keyframe-based frontend and backend. Its observability analysis is presented in Section IV. Simulation study on sensor parameter observability is reported in Section V. Section VI evaluates motion estimation and self-calibration on public benchmarks. Section VII summarizes the work and points out future directions.

II. RELATED WORK

Regarding observability analysis that underlies on-the-fly sensor calibration and real-time VIO methods that deals with degenerate motion, we briefly review investigations about camera-IMU-based sensor fusion.

A. Observability Analysis and Self-Calibration

As the camera-IMU systems are widely adopted, the necessity of calibration motivates the observability property analysis which has been explored from various aspects, usually with the

ORC of an observability matrix [24] constructed from either Jacobians of the linearized system (*e.g.*, [25], [26]) or gradients of Lie derivatives of the original nonlinear system (*e.g.*, [27], [13], [20], [15], [28]). Both types of ORC have revealed that the camera-IMU-based odometry in general has four unobservable directions, *i.e.*, the absolute translation and rotation about gravity [25], [29]. Free of approximation, the latter ORC approach lends itself to automated symbolic computation, thus capable of dealing with more complex systems.

Much effort has been devoted to the observability of sensor parameters which is the theoretical foundation for self-calibration. The camera extrinsic parameters are found in [27] to be observable when a calibration target is available. With natural features, the extrinsic parameters prove to be observable when at least two axes of the accelerometer and two axes of the gyroscope are excited (nonzero) [13]. Yang *et al.* [26] showed that the spatiotemporal parameters are observable with general motion by analyzing the linearized camera-IMU-based odometry system. They further presented that the IMU intrinsic parameters are observable when all axes of the IMU are excited [30]. The same conclusion was drawn in [15] for a stereo camera-IMU system by using Lie derivatives. The camera intrinsic parameters (excluding distortion) are shown to be observable in [14] under general motion. Though studies have shown that online calibration of the camera intrinsic, extrinsic, and IMU intrinsic parameters in combination is possible and beneficial to motion estimation [9], [16], a formal analysis of whether these parameters are observable is unavailable.

For the camera time offset to the IMU, it is asserted in [26] that it is only unobservable when the IMU experiences constant angular rate and linear acceleration. This assertion can also be interpreted from deductions in [31]. To our knowledge, the observability of temporal parameters in a VIO system has only been analyzed with a linearized system in [26] where the motion state variables are at variable times that depend on the time offset. Despite being conceptually simpler, the approach based on Lie derivatives has not been used to analyze temporal observability.

Regarding the above gaps, we conduct observability analysis of the VIO system with full self-calibration by using the Lie derivatives, revealing the observables in monocular camera-IMU and stereo camera-IMU setups.

B. Motion Estimation in Degenerate Motion

Two types of geometrical approaches for VIO are prevalent, those based on optimization, and filters. As some measurements arrive, an optimization-based approach conducts repeated linearizations and updates to refine the motion and structure variables. Example optimization-based VIO systems are OKVIS [11], VINS-Mono [32], and [33]. By contrast, a filter linearizes these measurements and updates the state variables and their covariance once, thereby saving much computation while supplying the covariance at no additional cost, especially suitable for low-cost systems [1].

The early VIO systems are often formulated as filters, *e.g.* [34], [35]. In the evolution of filters for VIO, the MSCKF

TABLE I
DIFFERENCES AND SIMILARITIES OF OUR WORK TO RELATED STUDIES.
RS: ROLLING SHUTTER. PROP.: PROPAGATION.

Methods	Ours	[11]	[9]	[32]	[10]
Supported setup	mono stereo	mono stereo	mono	mono	≥ 1 cameras
Keyframe-based frontend	✓	✓	×	×	×
Keyframe-based backend	✓	✓	×	✓	×
Standstill in mono setup	Work	Work	Fail	Work	Fail
Calibrated params	camera-IMU params	camera extrinsics	camera-IMU params	camera extrinsics, delay	camera extrinsics, intrinsics
Deal with RS effect	IMU prop.	N/A	IMU prop.	optic flow correction	interpol. by poses in state

proposed in [19] had been a milestone, enabling real-time motion estimation with a monocular camera-IMU setup. It had some bearing on many subsequent filtering approaches, *e.g.*, [36], [37], [12]. Among them, these methods [21], [20], [38], [39], [10] can be viewed as derivatives of MSCKF, enhancing it to be consistent and to deal with multiple cameras.

However, structureless filters that update motion estimates with every arrived image, *e.g.*, variants of MSCKF, are prone to drift during hovering or stationary periods. This issue was mitigated by switching to a last-in-first-out state management strategy in [8]. Later, ZUPT was adopted in [10]. These approaches require heuristics for motion detection which often are not portable. For instance, ZUPT may not work well with hovering.

To bridle drift of a structureless filter in degenerate motion, we leverage the concept of keyframes in both the feature association frontend and the state estimation backend.

Though keyframes have been widely adopted in optimization-based visual SLAM methods [40], *e.g.*, [11], [32], where the keyframe schemes help reduce computation in optimizing local maps, very few filters incorporate the keyframe concept perhaps because of efficiency in themselves. The VIO filters in [41], [39] used keyframe-based state management in the backend similar to VINS-Mono [32]. In [1], a preprocessing module selects a subset of frames as keyframes and poses of only keyframes are estimated in the backend inverse SWF. To deal with stationary periods, the EKF proposed in [42] keeps a cloned state variable for the latest keyframe in order to use for update epipolar constraints due to points observed in that keyframe and the current frame. Overall, our proposed KSWF shares features with [9], [11], [32], [10] to which the differences are summarized in Table I. In view of these studies, we believe that the proposed KSWF is the first keyframe-based filter that supports full self-calibration.

III. KEYFRAME-BASED SLIDING WINDOW FILTER WITH SELF-CALIBRATION

From two aspects, self-calibration and resilience to degeneration motion, this work studies the VIO problem, which is to track the pose (position and orientation) and optionally calibrate the sensor parameters of a platform consisting of an IMU and at least one camera using inertial readings and image observations of opportunistic landmarks with unknown positions. Considering both aspects, we propose the KSWF with self-calibration. It has two keyframe-based components: the feature association frontend which extracts feature matches from images, and the estimation backend which fuses feature matches and inertial measurements to estimate motion and optional parameters. Next, we present in turn notation conventions, IMU and camera measurement models, state variables, the frontend, and the backend filter.

A. Notation and Coordinate Frames

The Euclidean transformation from reference frame $\{B\}$ to $\{A\}$ is represented by a transformation matrix \mathbf{T}_{AB} which consists of a 3×3 rotation matrix \mathbf{R}_{AB} and a 3D translation vector \mathbf{p}_{AB}^A which is coordinates of $\{B\}$'s origin in $\{A\}$, *i.e.*, $\mathbf{T}_{AB} = \begin{bmatrix} \mathbf{R}_{AB} & \mathbf{p}_{AB}^A \\ \mathbf{0}^T & 1 \end{bmatrix}$. For brevity, we will write \mathbf{p}_{AB}^A as \mathbf{p}_{AB} or \mathbf{p}^A when its meaning is clear.

This work uses several right-handed coordinate frames, camera frames $\{C_k\}$, $k = 0, 1$, body frame $\{B\}$, and world frame $\{W\}$. The right-down-forward frame $\{C_k\}$ is affixed to the lens optical center of a camera k . Without loss of generality, we assign index 0 to the left camera of a stereo rig and refer to it as the main camera. $\{B\}$ is the frame affixed to the platform which estimated poses by a VIO method refer to. It is defined to have origin at the intersection of the accelerometer x and y input axes, and a known orientation \mathbf{R}_{BC_0} to the main camera. For easy result comparison, \mathbf{R}_{BC_0} is set to be the nominal orientation between the IMU and main camera. Moreover, a quasi-inertial world frame $\{W\}$ is instantiated at the start with accelerometer measurements such that its z -axis is along negative gravity.

B. IMU Measurements

To consider systematic and random errors in the three-axis gyroscope and accelerometer, we use an IMU model as in [9] which accounts for random biases and noises, and systematic errors (also known as IMU intrinsic parameters) including scale factor errors, misalignment, relative orientations, and g -sensitivity. This model is chosen to simplify the subsequent observability analysis.

The accelerometer measures the specific force applied to the IMU in $\{B\}$, \mathbf{a}_s^B . The measurement \mathbf{a}_m is affected by systematic errors encoded in a 3×3 matrix \mathbf{T}_a , accelerometer bias \mathbf{b}_a and noise process ν_a ,

$$\begin{aligned} \mathbf{a}_s^B &= \mathbf{R}_{WB}^T \cdot (\dot{\mathbf{v}}_{WB} - [0 \ 0 \ -g]^T) \\ \mathbf{a}_m &= \mathbf{T}_a \mathbf{a}_s^B + \mathbf{b}_a + \nu_a \\ \dot{\mathbf{b}}_a &= \nu_{ba}, \end{aligned} \quad (1)$$

where \mathbf{v}_{WB} is platform velocity in $\{W\}$, g is gravity magnitude and \mathbf{b}_a is assumed to be driven by Gaussian white noise process ν_{ba} . Nine entries of \mathbf{T}_a represent 3-DOF (degree-of-freedom) scale factor errors, 3-DOF misalignment, and 3-DOF orientation between accelerometer input axes and $\{B\}$.

The gyroscope measures angular rate of the platform in $\{B\}$, ω_{WB}^B . The measurement ω_m is affected by systematic errors encoded in a 3×3 matrix \mathbf{T}_g , g -sensitivity effect encoded in a 3×3 matrix \mathbf{T}_s , gyroscope bias \mathbf{b}_g , and noise process ν_g ,

$$\begin{aligned}\omega_m &= \mathbf{T}_g \omega_{WB}^B + \mathbf{T}_s \mathbf{a}_s^B + \mathbf{b}_g + \nu_g \\ \dot{\mathbf{b}}_g &= \nu_{bg}.\end{aligned}\quad (2)$$

where \mathbf{b}_g is assumed to be driven by Gaussian white noise process ν_{bg} . Nine entries of \mathbf{T}_g represent 3-DOF scale factor errors, 3-DOF misalignment, and 3-DOF orientation between gyroscope input axes and $\{B\}$. Here, \mathbf{T}_a and \mathbf{T}_g are fully populated for generality, but they may be simplified to be lower triangular given an alternative $\{B\}$ or extra knowledge of the IMU.

The power spectral densities of ν_a , ν_g , ν_{ba} , and ν_{bg} , are usually assumed to be $\sigma_a^2 \mathbf{I}_3$, $\sigma_g^2 \mathbf{I}_3$, $\sigma_{ba}^2 \mathbf{I}_3$, and $\sigma_{bg}^2 \mathbf{I}_3$, respectively, but they may have disparate diagonal values, and nonzero off-diagonal entries, *e.g.*, for a 2-DOF gyro.

To predict pose and velocity and their covariance, propagation with IMU data by the trapezoidal rule is carried out as described in [16, Appendix A], [43]. We also extend the propagation to support integration backward in time so as to predict camera poses for features in images captured by a RS camera. The propagation step uses the gravity norm provided by the user (1).

C. Camera Measurements

The proposed method supports image streams from one camera or two roughly synchronized cameras. In the stereo setup, two frames of the two cameras are grouped into a frame bundle when they have close timestamps per the camera clock. In a frame bundle of index j , we denote the original time of an image k , $k = 0, 1$, stamped by the camera clock, by t_j^{Ck} . Camera k 's clock has an offset t_d^k relative to the IMU clock. Then, the timestamp by the IMU clock for the central row of image k , t_j^k , is given by

$$t_j^k = t_j^{Ck} + t_d^k. \quad (3)$$

In the filter, state variables will be stamped by the estimated IMU time for the main camera's images. Suppose that the latest time offset estimate of the main camera as frame bundle j arrives is $t_{d,j}^0$, then the time for state variables associated with bundle j is set to a constant value t_j given by

$$t_j = t_j^{C0} + t_{d,j}^0. \quad (4)$$

With mid-exposure time of an image, we can compute the observation time per the IMU clock of any row in an image. Denote the frame readout time for camera k by t_r^k . Suppose

that a landmark i has an observation at row v in image k , then its timestamp $t_{i,j}^k$ is computed by

$$t_{i,j}^k = t_j^k + \left(\frac{v}{h} - \frac{1}{2}\right)t_r^k \quad (5)$$

where h is the height of image k . Using the central row of the RS image as the reference epoch instead of its first row reduces the average prediction horizon and hence computation when predicting camera poses with IMU data for landmark observations.

We use the conventional reprojection model for landmark observations in images. Consider a landmark \mathbf{L}_i observed in image k , $k = 0, 1$, of frame bundle j at $\mathbf{z}_{i,j}^k = [u, v]^T$, and denote the reprojection function of camera k by $\mathbf{h}^k(\cdot)$ which factors in all camera parameters, \mathbf{x}_C^k , including the camera extrinsic and intrinsic parameters, camera time offset t_d^k , and frame readout time t_r^k .

The reprojection model varies slightly depending on how the landmark is parameterized. If the landmark is expressed in $\{W\}$, $\mathbf{p}_i^W = [x_i, y_i, z_i, 1]^T$, the model is given by

$$\mathbf{z}_{i,j}^k = \mathbf{h}^k(\mathbf{T}_{BCk}^{-1} \mathbf{T}_{WB(t_{i,j}^k)}^{-1} \mathbf{p}_i^W) + \mathbf{w}_c \quad (6)$$

where $B(t_{i,j}^k)$ denotes the body frame at feature time $t_{i,j}^k$, and we assume that an image observation is affected by Gaussian noise $\mathbf{w}_c \sim N(\mathbf{0}, \sigma_c^2 \mathbf{I}_2)$. This reprojection model is used for observability analysis in Section IV for simplicity.

If landmark \mathbf{L}_i is anchored in image b , $b \in \{0, 1\}$, of frame bundle a , and represented with its inverse depth, the reprojection model will involve the body frame at bundle a 's assigned epoch t_a (4), $\{B(t_a)\}$. Now \mathbf{L}_i is expressed in the camera frame at t_a of image b , $\{C_b(t_a)\}$, *i.e.*, $\mathbf{p}_i^{C_b(t_a)} = \frac{1}{\rho_i}[\alpha_i, \beta_i, 1, \rho_i]^T$, with inverse depth ρ_i and observation direction $[\alpha_i, \beta_i, 1]$, the observation model is given by

$$\mathbf{z}_{i,j}^k = \mathbf{h}^k(\mathbf{T}_{BCk}^{-1} \mathbf{T}_{WB(t_{i,j}^k)}^{-1} \mathbf{T}_{WB(t_a)} \mathbf{T}_{BCb} \cdot \mathbf{p}_i^{C_b(t_a)}) + \mathbf{w}_c. \quad (7)$$

This model is used in our experiments because anchored landmark representation does not cause inconsistency [44].

For the camera observation, the estimator will need measurement Jacobians of $\mathbf{z}_{i,j}^k$. Among them, one key component is Jacobians of the pose at feature time $t_{i,j}^k$, $\mathbf{T}_{WB(t_{i,j}^k)}$, relative to the pose and velocity at state time t_j , $\mathbf{T}_{WB(t_j)}$ and $\mathbf{v}_{WB(t_j)}$, respectively. Both are computed along with IMU propagation from t_j to $t_{i,j}^k$. Jacobians relative to time parameters, *e.g.*, t_d^k , $k = 0, 1$, are computed with the propagated velocity $\mathbf{v}_{WB}(t_{i,j}^k)$ and fitted angular rate $\omega_{WB}^B(t_{i,j}^k)$. Jacobians relative to IMU parameters are ignored as in [45] because their entries are usually small (with first order terms up to $O(t_r)$).

Our estimation framework supports multiple camera models. When the camera intrinsic parameters are to be calibrated, we recommend using the pinhole radial tangential 8-parameter model [46] or the Kannala Brandt 6-parameter model [47] as the observability analysis in Section IV shows that their parameters are observable. Without loss of generality, we assume the pinhole radial tangential 8-parameter model (14) is used in the following unless otherwise stated.

TABLE II
STATE VARIABLES ESTIMATED BY KSWF FOR A STEREO CAMERA-IMU
SETUP. NOTE THAT \mathbf{R}_{C_0B} IS KNOWN AND THE PINHOLE RADIAL
TANGENTIAL MODEL IS ASSUMED.

State variables	Time-varying	Time-invariant
Motion	$\mathbf{T}_{WB(t)}, \mathbf{v}_{WB(t)}$	$\{\mathbf{T}_{WB(t_j)}, \mathbf{v}_{WB(t_j)}\}$ $j = 0, 1, \dots, N_{kf} + N_{tf} - 1$
IMU	$\mathbf{b}_g, \mathbf{b}_a$	$\mathbf{T}_g, \mathbf{T}_s, \mathbf{T}_a$
Camera	Time-invariant	
Extrinsics	$\mathbf{p}_{C_0B}, \mathbf{T}_{BC_1}$	
Intrinsics	$\{f_x^k, f_y^k, c_x^k, c_y^k, k_1^k, k_2^k, p_1^k, p_2^k\}, k = 0, 1$	
Time offset	$t_r^k, k = 0, 1$	
Readout time	$t_d^k, k = 0, 1$	

D. State Variables in the Filter

The state vector of the KSWF at time t , $\mathbf{x}(t)$, consists of current navigation state variable $\boldsymbol{\pi}(t)$, IMU parameters \mathbf{x}_S , parameters of N cameras \mathbf{x}_C , and a sliding window of past navigation state variables \mathbf{x}_W at known epochs $\{t_j\}$ where j enumerates N_{kf} keyframe bundles and N_{tf} recent temporal frame bundles, and landmarks \mathbf{x}_L . That is,

$$\mathbf{x}(t) = \{\boldsymbol{\pi}(t), \mathbf{x}_S, \mathbf{x}_C, \mathbf{x}_W, \mathbf{x}_L\} \quad (8)$$

$$\boldsymbol{\pi}(t) = \{\mathbf{p}_{WB}(t), \mathbf{R}_{WB}(t), \mathbf{v}_{WB}(t)\} \quad (9)$$

$$\mathbf{x}_S = \{\mathbf{b}_g(t), \mathbf{b}_a(t), \vec{\mathbf{T}}_g, \vec{\mathbf{T}}_s, \vec{\mathbf{T}}_a\} \quad (10)$$

$$\mathbf{x}_C = \{\mathbf{x}_C^k | k = 0, 1\} \quad (11)$$

$$\mathbf{x}_W = \{\boldsymbol{\pi}(t_j) | j = 0, 1, \dots, N_{kf} + N_{tf} - 1\} \quad (12)$$

$$\mathbf{x}_L = \{\mathbf{L}_i | i = 0, 1, \dots\} \quad (13)$$

where $(\vec{\cdot})$ concatenates rows of a matrix into a vector.

The extrinsic parameters of the main camera, \mathbf{T}_{C_0B} , has a preset known rotation \mathbf{R}_{BC_0} , therefore, for a monocular camera-IMU setup, the camera parameters suitable for calibration are

$$\mathbf{x}_C = \{\mathbf{p}_{C_0B}, f_x^0, f_y^0, c_x^0, c_y^0, k_1^0, k_2^0, p_1^0, p_2^0, t_d^0, t_r^0\} \quad (14)$$

For the second camera, its extrinsic variable is parameterized by \mathbf{T}_{BC_1} . Parameters that can be estimated by the filter for a stereo camera-IMU setup are listed in Table II.

Each navigation state in the sliding window $\boldsymbol{\pi}(t_j)$ associated with frame bundle j is at a known epoch t_j (4). Tying navigation state variables to known epochs is conceptually simpler than tying them to true epochs which are uncertain as in [10], [45]. The past navigation variables also include velocity so that the RS camera pose for a landmark observation can be propagated from the relevant navigation state variable with IMU measurements.

Camera parameters \mathbf{x}_C and IMU intrinsic parameters are assumed to be unknown constants as in [9], [10], as they change little in the timespan of the sliding window. However, if a sensor parameter is in fact not constant, noise can be added to account for its drift over time as done for IMU biases.

The error $\delta\mathbf{x}$ for a state variable \mathbf{x} in a vector space is defined to be $\mathbf{x} = \hat{\mathbf{x}} + \delta\mathbf{x}$, where $\hat{\mathbf{x}}$ is its estimate. For the

rotation matrices on a Lie group, the error state is defined by the Lie algebra. For example, \mathbf{R}_{WB} 's error state $\delta\boldsymbol{\theta}_{WB}$ is defined by $\mathbf{R}_{WB} = \exp(\delta\boldsymbol{\theta}_{WB}^\times) \hat{\mathbf{R}}_{WB} \approx (\mathbf{I} + \delta\boldsymbol{\theta}_{WB}^\times) \hat{\mathbf{R}}_{WB}$, where $(\cdot)^\times$ obtains the skew-symmetric matrix of a 3D vector.

E. Feature Association Frontend

The frontend extracts image features by using descriptors, e.g., BRISK [48], and matches descriptors from the current frame bundle to the last bundle as well as several previous keyframe bundles, similarly to [11], as illustrated in Fig. 1.

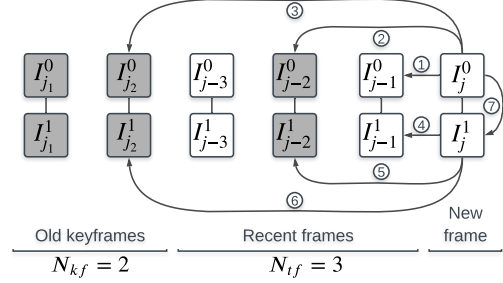


Fig. 1. The keyframe-based feature matching consists of matching the current frame bundle to the last frame bundle, ① and ④, matching the current frame bundle to two previous keyframe bundles, ②, ③, ⑤, and ⑥, and matching between images of the current frame bundle, ⑦. Showing keyframe bundles as shaded frame bundles, this diagram assumes a platform with stereo cameras. For a single camera setup, only ①–③ are needed.

The frontend distinguishes ordinary frame bundles and keyframe bundles by using the view overlap criteria in [11]. For every image k , $k = 0, 1$, in the current frame bundle, among its features \mathcal{F}_k , we find those associated with feature tracks in existing keyframe bundles, \mathcal{M}_k . Then, we compute the overlap o_k between the convex hull of \mathcal{M}_k and that of \mathcal{F}_k , and the ratio r_k between $|\mathcal{M}_k|$ and the number of features in image k , $|\mathcal{F}_k|$. A keyframe bundle is selected if the maximum of area overlaps $\{o_k | k \in [0, 1]\}$ is less than a threshold T_o (typically 60%) or if the maximum of match ratios $\{r_k | k \in [0, 1]\}$ is less than T_r (typically 20%).

F. Filter Workflow

The backend of KSWF estimates state variables tied to frame and keyframe bundles using feature observations and marginalizes redundant state variables (Fig. 2). The filter manages motion-related state variables depending on whether they are associated with keyframe bundles. The keyframe-based state management scheme is facilitated by the selection of keyframe bundles in the frontend.

The proposed filter is outlined in Algorithm 1. At the start, the VIO system is initialized to zero position, zero velocity, and an orientation such that z -axis of $\{W\}$ is along negative gravity by using a few accelerometer data. Note that since the filter enforces this condition, the initial coarse orientation will be refined subsequently. The biases are set by averaging the IMU data if the optic flow relative to the first frame is small. Otherwise, they are set to zero. We did not use advanced initialization strategies of e.g., [32], [6] which in our experience worked well with calibrated cameras

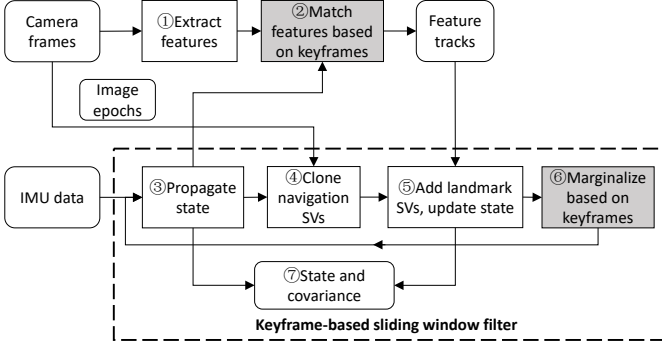


Fig. 2. Flowchart of the keyframe-based sliding window filter. SV: state variable. ①-② are touched on in III-E. ③-⑥ are presented in III-F. ⑦ is described in III-D.

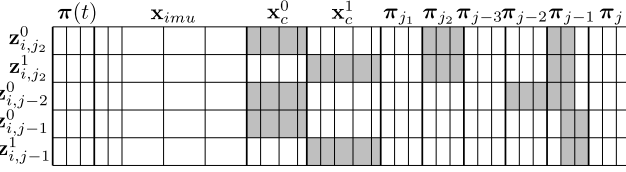


Fig. 3. Schematic drawing of a landmark i 's observation Jacobians relative to the state vector whose nonzero entries are shaded. For clarity, the landmark is assumed not in the state. In accordance with Fig. 1, as a new frame bundle j arrives, this landmark completes its feature track at frame bundle $j-1$ which serves as its anchor frame bundle (7). After the navigation state variable for frame bundle j has been cloned as $\pi_j := \pi(t_j)$, the computed Jacobians for i are stacked as shown and ready for canceling out the Jacobian for i 's parameters (Section III-F).

but poorly with inaccurate calibration. Remaining IMU and camera parameters are initialized to values from datasheets or experience. The standard deviations of state variables are initialized to sensible values (see Table IV for simulation).

As a frame bundle j arrives, the navigation state $\pi(t)$ and the covariance matrix are propagated with IMU data to the state epoch t_j (Box ③ of Fig. 2). Then, $\pi(t)$ is cloned and appended to the state vector and the covariance matrix is also expanded for the cloned $\pi(t_j)$ (Line 3, Box ④ of Fig. 2). As $\pi(t_j)$ is at a known epoch t_j , unlike [10] or [45, (30)], we need not to account for uncertainty in its time when augmenting covariance for $\pi(t_j)$. Instead, we need to compute the measurement Jacobian relative to camera time offsets in the update step (Line 12).

In parallel, feature descriptors are extracted from images of bundle j and matched to those of the last bundle $j-1$ and several recent keyframe bundles (e.g., bundle $j-2$ and j_2 in Fig. 1). After that, three types of feature tracks will be used for update: tracks that disappear in bundle j , observations of landmarks in the state vector, and tracks that can triangulate a new landmark to the state. They differ in how to prepare for the update. For disappeared tracks, Jacobians relative to landmark parameters need to be canceled out by matrix nullspace projection [19]. For the third type, triangulated new landmarks will be augmented to the state and covariance. For all three observation types, the update is carried out identical to the classic EKF [43], [16]. It is possible to use an iterated update scheme for disappeared features. However, empirically,

despite additional computation, its improvement on accuracy across datasets was marginal [12].

For a landmark i , stacked Jacobians of its observations relative to the state vector are visualized in Fig. 3. For a landmark with large depth, the observation Jacobian relative to its parameters (i.e., the landmark Jacobian) can be rank-deficient, and the fact should be considered in canceling out the landmark Jacobian and in performing the following Mahalanobis gating test.

To bound computation, redundant frame bundles are selected and marginalized from the filter (Lines 25-27, Box ⑥ of Fig. 2), once the number of navigation state variables in the sliding window exceeds $N_{kf} + N_{tf}$. In a marginalization operation, at least N_r redundant bundles (N_r is 3 for a monocular setup, 2 for a stereo setup) are chosen (Line 25) since two reprojection measurements for an unknown landmark is uninformative [39]. To meet this requirement, redundant bundles are chosen first among the recent non-keyframe bundles while excluding the most recent N_{tf} bundles and secondly among the oldest keyframe bundles. For the case of Fig. 1, $N_{kf} = 2$ and $N_{tf} = 3$, the redundant bundles for the latest bundle j are keyframe bundle j_1 and frame bundle $j-3$.

With these redundant bundles, we update the filter with observations of landmarks each observed more than twice in these bundles (Line 26). For such a landmark, if it can be triangulated with its entire observation history, its observations in the redundant bundles are used for EKF update. Other observations in the redundant bundles are discarded. After the update, state variables and entries in the covariance matrix for these redundant bundles are removed (Line 27).

To ensure filter consistency, for IMU propagation and camera measurements, Jacobians are evaluated at propagated values of position and velocity, i.e., first estimates [21], and at the latest estimates of other variables, e.g., IMU biases, landmarks expressed by anchored inverse depth, since they do not affect the unobservable directions [44].

IV. OBSERVABILITY ANALYSIS

By using the ORC of Lie derivatives, this section shows that the VIO system with self-calibration is weakly observable under general motion while excluding the four immanent unobservable dimensions. We first review the basics of observability analysis with Lie derivatives. Then, this method is applied to the monocular global shutter (GS) camera-IMU-based odometry with self-calibration while ignoring time variables. Discussions on extensions are also given. Lastly, we consider observability of time offset and RS readout time.

A. Observability Analysis Fundamentals

According to [28], a state at time t_0 , $\mathbf{x}(t_0)$, is weakly observable if there is a neighborhood in which all its neighbors can be distinguished from itself by the knowledge of outputs and user-chosen inputs in a time interval $\mathcal{I} = [t_0, t_0 + T]$. For a noise-free system that is affine in the control inputs \mathbf{u}_i , $i = 1, 2, \dots, p$,

$$\dot{\mathbf{x}} = \mathbf{f}_0(\mathbf{x}) + \sum_{i=1}^p \mathbf{f}_i(\mathbf{x})\mathbf{u}_i, \quad \mathbf{y} = \mathbf{h}(\mathbf{x}) \quad (15)$$

Algorithm 1 KSWF workflow.

```

1: Initialize state and covariance
2: while a frame bundle  $j$  arrives do
3:   Propagate state variable  $\pi(t)$  to  $t_j$  with IMU data
4:   Augment covariance for the cloned state variable  $\pi(t_j)$ 
5:   Extract descriptors and match to the last frame bundle
   and previous keyframe bundles
6:   for disappeared feature tracks do
7:     Triangulate the point landmark
8:     Compute residuals and Jacobians of reprojection
   errors
9:     Cancel out Jacobians for the landmark
10:    Remove outliers with Mahalanobis test
11:   end for
12:   Update state and covariance
13:   for feature tracks of landmarks in state do
14:     Compute residuals and Jacobians of reprojection
   errors
15:     Remove outliers with Mahalanobis test
16:   end for
17:   Update state and covariance
18:   for feature tracks of well-observed landmarks but not
   in state do
19:     Triangulate the point landmark
20:     Compute residuals and Jacobians of reprojection
   errors
21:     Remove outliers with Mahalanobis test
22:   end for
23:   Augment state and covariance for these landmarks
24:   Update state and covariance
25:   if Redundant frame bundles are detected then
26:     Update with features in these frame bundles  $\triangleright$  As
   with the disappeared features
27:   Remove associated state variables and covariance
   entries
28:   end if
29: end while

```

the sufficient condition for weak observability of its state \mathbf{x} is that the observability matrix built from the outputs $\mathbf{h}(\mathbf{x})$ has full rank [22], [28]. The observability matrix \mathcal{O} consists of gradients of Lie derivatives of $\mathbf{h}(\mathbf{x})$ along vector fields \mathbf{f}_i of the control inputs \mathbf{u}_i . For a vector output function \mathbf{h} , its first order Lie derivative along the vector field $\mathbf{f}_i = [\mathbf{f}_{i1} \ \mathbf{f}_{i2} \ \cdots \ \mathbf{f}_{is}]$ of s columns is defined by

$$\mathcal{L}_{\mathbf{f}_i}^1 \mathbf{h} = \begin{bmatrix} \nabla \mathbf{h} \cdot \mathbf{f}_{i1} \\ \nabla \mathbf{h} \cdot \mathbf{f}_{i2} \\ \vdots \\ \nabla \mathbf{h} \cdot \mathbf{f}_{is} \end{bmatrix} \quad (16)$$

The zeroth order Lie derivative is defined to be

$$\mathcal{L}^0 \mathbf{h} = \mathbf{h}. \quad (17)$$

Higher order Lie derivatives can be computed recursively by

$$\mathcal{L}_{\mathbf{f}_i, \mathbf{f}_j}^2 \mathbf{h} = \mathcal{L}_{\mathbf{f}_j}^1 \mathcal{L}_{\mathbf{f}_i}^1 \mathbf{h}. \quad (18)$$

With these Lie derivatives of the observation function, the entire observability matrix \mathcal{O} is given by

$$\mathcal{O} = \begin{bmatrix} \nabla \mathcal{L}^0 \mathbf{h} \\ \nabla \mathcal{L}_{\mathbf{f}_i}^1 \mathbf{h} \\ \nabla \mathcal{L}_{\mathbf{f}_i, \mathbf{f}_j}^2 \mathbf{h} \\ \vdots \end{bmatrix}, \quad (19)$$

where $i, j = [0, 1, \dots, p]$. \mathcal{O} can be viewed as a codistribution spanned by row vectors (also known as covectors). That is, \mathcal{O} can be written as

$$\mathcal{O} = \text{span}\{\nabla \mathcal{L}^0 \mathbf{h}, \nabla \mathcal{L}_{\mathbf{f}_i}^1 \mathbf{h}, \nabla \mathcal{L}_{\mathbf{f}_i, \mathbf{f}_j}^2 \mathbf{h}, \dots\} \quad (20)$$

The observability property of the affine-input system can be revealed by incrementally building up the codistribution and checking its dimension. Denote the codistribution with gradients of Lie derivatives up to order k by \mathcal{O}_k , *e.g.*, $\mathcal{O}_0 = \text{span}\{\nabla \mathbf{h}\}$ and $\mathcal{O}_1 = \text{span}\{\nabla \mathbf{h}, \nabla \mathcal{L}_{\mathbf{f}_0}^1 \mathbf{h}, \nabla \mathcal{L}_{\mathbf{f}_1}^1 \mathbf{h}, \dots, \nabla \mathcal{L}_{\mathbf{f}_p}^1 \mathbf{h}\}$. As deduced in [28, Algorithm 4.1], if $\text{rank}(\mathcal{O}_{k-1}) = \text{rank}(\mathcal{O}_k)$, the incremental procedure completes. By then, if $\text{rank}(\mathcal{O}_k) = \dim(\mathbf{x})$, the system is weakly observable.

To simplify observability analysis, it is beneficial to proactively identify observable dimensions of the state \mathbf{x} in building up the codistribution. Considering the codistribution at step k , \mathcal{O}_k , this can be done with two equivalent techniques. By [24, Corollary 2.1], a component of \mathbf{x} , \mathbf{x}_i , is weakly observable if removing the column corresponding to \mathbf{x}_i from \mathcal{O}_k reduces its rank by 1. Alternatively, according to [28, Theorem 4.8], \mathbf{x}_i is weakly observable if the unit covectors $\nabla \mathbf{x}_i$ belongs to the codistribution \mathcal{O}_k , *i.e.*, adding covectors $\nabla \mathbf{x}_i$ to \mathcal{O}_k does not increase its rank.

B. Weak Observability without Time Parameters

This section investigates whether state variables of the monocular GS camera-IMU-based odometry with self-calibration are weakly observable using observations from an unknown point landmark, except the well-known four unobservable directions. The below analysis easily extends to multiple point landmarks without changing the conclusions.

To ease analysis, the system is expressed by an alternative set of variables which is deliberately chosen to be real and non-trigonometric to avoid reporting false larger ranks of matrices. We begin with the IMU parameters. Ignoring noises, the calibrated IMU measurements are computed by

$$\begin{aligned} \mathbf{a}_t &= \underbrace{\mathbf{T}_a^{-1}}_{\mathbf{M}_a} (\mathbf{a}_m - \mathbf{b}_a) \\ \boldsymbol{\omega}_t &= \underbrace{\mathbf{T}_g^{-1}}_{\mathbf{M}_g} \boldsymbol{\omega}_m - \underbrace{\mathbf{T}_g^{-1} \mathbf{b}_g}_{\mathbf{b}'_g} - \underbrace{\mathbf{T}_g^{-1} \mathbf{T}_s \mathbf{T}_a^{-1}}_{\mathbf{M}_s} (\mathbf{a}_m - \mathbf{b}_a) \end{aligned} \quad (21)$$

where the fully populated matrices \mathbf{M}_a , \mathbf{M}_g , \mathbf{M}_s , and \mathbf{b}'_g are substitutes for \mathbf{T}_a , \mathbf{T}_g , \mathbf{T}_s , and \mathbf{b}_g , respectively. Next, the unknown landmark \mathbf{L}_i is represented by inverse depth ρ and direction γ in the camera frame $\{C\}$. That is,

$$\gamma = [\gamma_1, \gamma_2]^T = [p_{i,x}^C / p_{i,z}^C, p_{i,y}^C / p_{i,z}^C]^T, \quad \rho = 1 / p_{i,z}^C, \quad (22)$$

where $[p_{i,x}^C \ p_{i,y}^C \ p_{i,z}^C]$ are time-varying coordinates of the landmark in $\{C\}$. Moreover, we use the gravity vector \mathbf{g}^B

expressed in $\{B\}$ to encode gravity magnitude, and roll and pitch of the camera-IMU system. Overall, the system state is

$$\mathbf{x} = \{\gamma, \rho, \mathbf{v}^B, \mathbf{g}^B, \mathbf{b}'_g, \mathbf{b}_a, \tilde{\mathbf{M}}_g, \tilde{\mathbf{M}}_s, \tilde{\mathbf{M}}_a, \mathbf{x}_C\} \quad (23)$$

where $\mathbf{x}_C = \{\mathbf{p}_{CB}, f_x, f_y, c_x, c_y, k_1, k_2, p_1, p_2\}$, excluding temporal parameters t_d^0 and t_r^0 and dropping the camera index 0 from superscripts for brevity. Comparing to (8), we see that the alternative system state covers all variables in the original monocular VIO system except $t_d^0, t_r^0, \mathbf{p}_{WB}$, and yaw. The state dimension is $\dim(\mathbf{x}) = 53$.

Assuming that biases are constant in a short timespan, with basic derivations, the system model is found to be

$$\begin{aligned} \begin{bmatrix} \dot{\gamma} \\ \dot{\rho} \\ \dot{\mathbf{v}}^B \\ \dot{\mathbf{g}}^B \end{bmatrix} &= \begin{bmatrix} C_{\gamma\rho}[(\mathbf{R}_{CB}\boldsymbol{\omega}_t) \times (\rho\mathbf{p}_{CB} - \bar{\gamma}) - \mathbf{R}_{CB}\rho\mathbf{v}^B] \\ \mathbf{v}^B \times \boldsymbol{\omega}_t + \mathbf{a}_t + \mathbf{g}^B \\ \mathbf{g}^B \times \boldsymbol{\omega}_t \end{bmatrix} \\ &= \mathbf{f}_0 + \mathbf{f}_1\mathbf{a}_m + \mathbf{f}_2\boldsymbol{\omega}_m \\ \dot{\mathbf{b}}'_g &= \dot{\mathbf{b}}_a = \mathbf{0}_{3 \times 1} \\ \dot{\tilde{\mathbf{M}}}_g &= \dot{\tilde{\mathbf{M}}}_s = \dot{\tilde{\mathbf{M}}}_a = \mathbf{0}_{3 \times 3}, \quad \dot{\mathbf{x}}_C = \mathbf{0}_{11 \times 1} \end{aligned} \quad (24)$$

where the shorthand notations are

$$\bar{\gamma} = [\gamma^T \quad 1]^T, \quad C_{\gamma\rho} = \begin{bmatrix} \mathbf{I}_2 & -\gamma \\ \mathbf{0}_{1 \times 2} & -\rho \end{bmatrix}. \quad (25)$$

To save space, the coefficient vector fields \mathbf{f}_i , $i = 0, 1, 2$ are not expanded. The known \mathbf{R}_{CB} is expressed by $[q_x, q_y, q_z, 1]^T$.

There are two types of observations to the system, point observation \mathbf{h}_1 , and gravity magnitude h_2 ,

$$\mathbf{h}_1 = \begin{bmatrix} f_x[\gamma_1(1 + k_1r^2 + k_2r^4) + 2p_1\gamma_1\gamma_2 + p_2(r^2 + 2\gamma_1^2)] + c_x \\ f_y[\gamma_2(1 + k_1r^2 + k_2r^4) + p_1(r^2 + 2\gamma_2^2) + 2p_2\gamma_1\gamma_2] + c_y \end{bmatrix} \quad (26)$$

$$h_2 = (\mathbf{g}^B)^T \mathbf{g}^B \quad (27)$$

where $r^2 = \gamma^T \gamma$.

We analyze the system of (24), (26), and (27) by incrementally constructing codistributions. With first order Lie derivatives, we find $\text{rank}(\mathcal{O}_1) = 17$. With second order Lie derivatives, $\text{rank}(\mathcal{O}_2) = 46$. By using the two deduction techniques, we identify that eight parameters of the pinhole radial tangential model, \mathbf{M}_g , and \mathbf{M}_s , are weakly observable. The same procedure shows that the FOV 5-parameter model [49], the extended unified camera 6-parameter model [50], and the Kannala Brandt 6-parameter model [47] are weakly observable with the second order codistribution \mathcal{O}_2 .

As a result, we can replace \mathbf{h}_1 with $\mathbf{h}'_1 = \gamma$ and remove camera intrinsic parameters from \mathbf{x} , giving a shorter state vector \mathbf{x}' , greatly simplifying the arduous analysis. For the new system, the third order codistribution has full rank, $\text{rank}(\mathcal{O}_3) = 45 = \dim(\mathbf{x}')$, implying that the system is weakly observable. One set of covectors spanning \mathcal{O}_3 is given by

$$\begin{aligned} \mathcal{O}_3 = \text{span}\{ & \nabla \mathcal{L}^0 \mathbf{h}_1, \nabla \mathcal{L}^0 h_2, \nabla \mathcal{L}^1_{f_0} \mathbf{h}_1, \nabla \mathcal{L}^1_{f_1} \mathbf{h}_1, \\ & \nabla \mathcal{L}^1_{f_2} \mathbf{h}_1, \nabla \mathcal{L}^2_{f_0, f_0} \mathbf{h}_1, \nabla \mathcal{L}^2_{f_1, f_0} \mathbf{h}_1, \nabla \mathcal{L}^2_{f_2, f_0} h_{11}, \\ & \nabla \mathcal{L}^2_{f_0, f_{11}} \mathbf{h}_1, \nabla \mathcal{L}^2_{f_{11}, f_{11}} h_{11}, \nabla \mathcal{L}^2_{f_0, f_{12}} \mathbf{h}_1, \\ & \nabla \mathcal{L}^2_{f_0, f_{13}} \mathbf{h}_1, \nabla \mathcal{L}^2_{f_0, f_{21}} \mathbf{h}_1, \nabla \mathcal{L}^2_{f_0, f_{22}} h_{11}, \\ & \nabla \mathcal{L}^3_{f_0, f_0, f_0} \mathbf{h}_1, \nabla \mathcal{L}^3_{f_{11}, f_0, f_0} h_{11}, \nabla \mathcal{L}^3_{f_0, f_{11}, f_0} h_{11}, \\ & \nabla \mathcal{L}^3_{f_0, f_{12}, f_0} h_{11}, \nabla \mathcal{L}^3_{f_0, f_{13}, f_0} h_{11}, \nabla \mathcal{L}^3_{f_0, f_0, f_{11}} h_{11} \} \end{aligned} \quad (28)$$

where $\mathbf{h}_1 \triangleq [h_{11}, h_{12}]^T$. The 45-row spanning set involves Lie derivatives computed along vector fields of all control inputs, \mathbf{a}_m and $\boldsymbol{\omega}_m$, implying that weak observability of the system requires that all six axes of the IMU are excited at some time of the interval \mathcal{I} .

C. Discussions on Extensions

It is worth noting that the known gravity magnitude is needed for calibrating scale factors of the accelerometer. If h_2 is unavailable, the system of (24) and (26) is identifiable up to a metric scale with the unobservable direction

$$\mathbf{N} = \begin{bmatrix} \mathbf{0}_2^T & -\rho & \mathbf{v}^{B^T} & \mathbf{g}^{B^T} & \mathbf{0}_{24}^T & \tilde{\mathbf{M}}_a^T & \mathbf{p}_{CB}^T & \mathbf{0}_8^T \end{bmatrix}^T \quad (29)$$

which satisfies $\mathcal{O}_k \mathbf{N} = \mathbf{0}$.

Also, if we assume one component of \mathbf{R}_{CB} is unknown, say q_x , then in the system of \mathbf{h}' and \mathbf{x}' , the number of unknowns becomes 46, but $\text{rank}(\mathcal{O}_3) = \text{rank}(\mathcal{O}_4) = 45$, meaning that the 3-DOF \mathbf{R}_{CB} is unobservable.

For the case of stereo cameras, if the IMU is unavailable, it is easy to show that the intrinsic and extrinsic parameters of the stereo camera rig (of dimension 22) are observable given 4D observations of 21 landmarks and the baseline length. Otherwise, for the stereo camera-IMU system, following the above analysis based on Lie derivatives, it can be shown that the intrinsic and extrinsic parameters of both cameras and the IMU intrinsic parameters as listed in Table II are observable given 4D observations of an unknown landmark and the gravity magnitude or the baseline length. Intuitively, one of the two latter constraints resolves the scale ambiguity.

When the system is standstill, whether at the beginning or middle of estimation, all state variables turn into unknown constants. None of them can be resolved given the set of observation equations because the Jacobian of these equations is rank deficient, unless some parameters are assumed well estimated. For instance, the IMU biases can be estimated if \mathbf{T}_g , \mathbf{T}_s , \mathbf{T}_a , and \mathbf{g}^W are roughly known. Moreover, the system pose can be obtained given sufficient observations of landmarks of roughly known positions along with the camera intrinsic parameters.

D. Observability of Time Parameters

Next, we deduce that in general the camera time offset of the VIO system can be estimated, that is, $\mathbf{h}(\mathbf{x}(t + t_d)) \neq \mathbf{h}(\mathbf{x}(t))$. To this end, we identify the conditions under which $\mathbf{h}(\mathbf{x}(t + t_d)) = \mathbf{h}(\mathbf{x}(t))$, and show that they are unlikely to occur.

By expanding the Taylor series for $\mathbf{h}(\mathbf{x}(t + t_d))$ in terms of $\mathbf{x}(t)$ and $\mathbf{u}_i(t)$ (Appendix A), we identify the following condition that leads to unobservable time offset,

$$\mathcal{O} \cdot \dot{\mathbf{x}} = \mathbf{0}, \quad \mathbf{a}_m = \text{const}, \quad \boldsymbol{\omega}_m = \text{const}. \quad (30)$$

This condition means that time offset becomes unobservable under constant inputs and when some other state variables are unobservable, i.e., \mathcal{O} is rank deficient. For instance, when the platform rotates about direction of the only feature with constant rate, and both the constant applied force and gravity are along the feature direction. Both [31] and [26] have

also found that time offset may become unobservable under constant inputs. These situations are unlikely to occur in practice.

Finally, we remark that the frame readout time can be obtained as long as the other sensor parameters can be estimated. We can choose an observation $\mathbf{z}_{i,j}^k$ of landmark \mathbf{L}_i , given the image k 's timestamp, the frame readout time can be solved for by a Newton-Raphson method.

In summary, the state in the VIO system (24), camera time offset, and readout time can be estimated under general motion. These variables correspond to the state variables of the monocular KSWF (8) except global translation and rotation about gravity, meaning that KSWF with self-calibration is feasible in theory.

V. SIMULATION STUDY

By simulation, this section shows that the presented sensor parameters can be estimated with observations of opportunistic point landmarks, and that the proposed KSWF can accurately estimate platform motion with inaccurately calibrated sensors.

The first scenario was setup with a monocular RS camera-IMU system and an artificial scene of points distributed on four walls. The camera-IMU platform traversed the scene for five minutes with a wavy circle motion (Fig. 4 top) at average velocity 1.26 m/s . For the second scenario, both the trajectory of the monocular camera-IMU system and the landmarks were generated from the TUM VI corridor1 dataset [51] by using the visual inertial mapping package, maplab [52], and B-spline fitting, as shown at the bottom of Fig. 4. For both setups, the camera of diagonal FOV 103° captured 752×480 images at 10 Hz and the IMU captured data at 100 Hz. Image observations were projected with the pinhole radial tangential model and affected by white Gaussian noise with standard deviation of 1 pixel at each dimension. The RS effect was simulated by solving for the feature observation time (5) as a root of the projection model (6). IMU data were affected by biases, bias random walk, and additive white noise. IMU noise parameters were chosen to be realistic for a consumer-grade IMU and are given in Table III. Sensor parameters used to simulate images and inertial data were set to mean values in Table IV.

A simulation frontend was created to associate landmark observations between consecutive frames and between a frame and its previous three keyframes. The average feature track length is 6.8 for the first scenario and 4.8 for the second one, and the average number of observed landmarks in an image is 60.5 for the first scenario and 175.6 for the second one.

We first study the effect of self-calibration with the first simulation setup. Four settings of KSWF with varying degrees of self-calibration were chosen: no calibration, calibrating IMU intrinsic parameters, calibrating camera intrinsic parameters and t_d and t_r (camera index 0 dropped for brevity), and the default full calibration. To evaluate motion estimation, comparison was made to OKVIS [11] and a structureless KSWF (SL-KSWF) which uses observations for update as a feature track disappears and does not add landmarks to the state vector. Note that for OKVIS, RS effect and camera time offset was not added in simulating data.

TABLE III
IMU NOISE PARAMETERS.

σ_{bg}	σ_{ba}	σ_g	σ_a
$2 \cdot 10^{-5}$	$5.5 \cdot 10^{-5}$	$1.2 \cdot 10^{-3}$	$8 \cdot 10^{-3}$
$\text{rad/s}^2/\sqrt{\text{Hz}}$	$\text{m/s}^3/\sqrt{\text{Hz}}$	$\text{rad/s}/\sqrt{\text{Hz}}$	$\text{m/s}^2/\sqrt{\text{Hz}}$

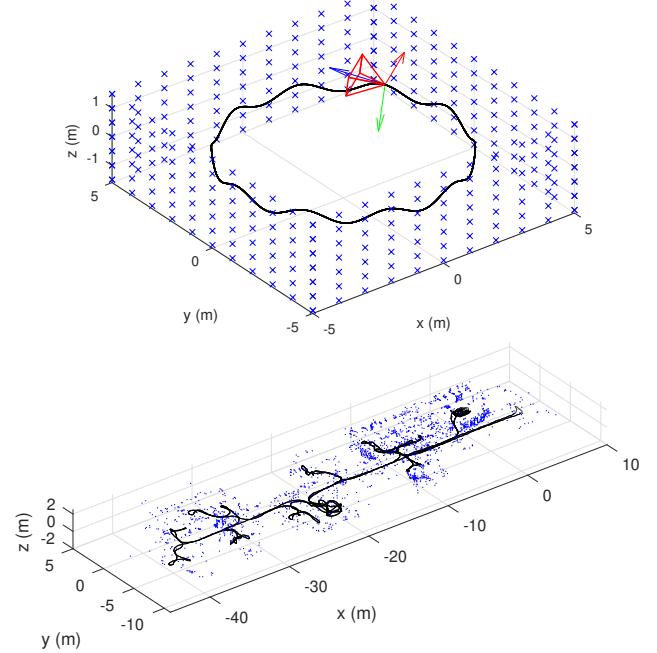


Fig. 4. Simulated setups for the monocular camera-IMU system. Top: Landmarks on walls and general wavy trajectory of the system. Bottom: Scene and trajectory generated from the TUM VI corridor1 dataset [51].

The compared estimators were initialized with true pose and true velocity affected by Gaussian noise $N(\mathbf{0}, 0.05^2 \mathbf{I}_3 \text{ m}^2/\text{s}^4)$. For KSWF, the initial values for sensor parameters were drawn from Gaussian distributions given in Table IV. A landmark was added to the state vector if it had been observed six times. OKVIS was initialized with either sensor models used in simulation or inaccurate sensor models. For the former, sensor parameters were initialized with mean values in Table IV except time delay and readout time which were set zero. For

TABLE IV
MEAN VALUES AND STANDARD DEVIATIONS σ AT EACH DIMENSION OF IMU AND CAMERA PARAMETERS USED TO SIMULATE DATA AND INITIALIZE ESTIMATORS. METRIC UNITS ARE USED UNLESS NOTED.

	$\mathbf{b}_g(^{\circ}/\text{s})$	\mathbf{b}_a	\mathbf{T}_g	\mathbf{T}_s	\mathbf{T}_a
Mean	$\mathbf{0}$	$\mathbf{0}$	\mathbf{I}_3	$\mathbf{0}_{3 \times 3}$	\mathbf{I}_3
σ	0.29	0.02	0.005	0.001	0.005
	\mathbf{R}_{CB}	$\mathbf{t}_{CB}(\text{cm})$	f_x, f_y $c_x, c_y (\text{px})$	k_1, k_2 p_1, p_2	t_d, t_r (ms)
Mean	$\begin{bmatrix} 0 & -1 & 0 \\ 0 & 0 & -1 \\ 1 & 0 & 0 \end{bmatrix}$	$\mathbf{0}$	350, 360 378, 238	0, 0 0, 0	20, 20
σ	0	2.0	2.0, 2.0 2.0, 2.0	0.05, 0.01 $10^{-3}, 10^{-3}$	5, 5

TABLE V
RMSE AT THE END OF 5-MINUTE WAVY MOTION FOR OKVIS, SL-KSWF, AND KSWF WITH VARYING LEVELS OF SELF-CALIBRATION, COMPUTED OVER SUCCESSFUL RUNS OF 100 ATTEMPTS WHICH WERE DEEMED SUCCESSFUL IF THE POSITION ERROR AT THE END IS <100 M.

Method	RMSE		Success runs
	\mathbf{p}_{WB} (m)	\mathbf{R}_{WB} ($^\circ$)	
OKVIS	0.49	6.82	100
OKVIS inaccurate calib	13.94	39.79	85
KSWF calib off	38.32	40.42	60
KSWF calib camera	2.00	18.18	100
KSWF calib IMU	30.73	40.55	69
KSWF full calib	0.23	1.22	100
SL-KSWF full calib	0.61	5.60	100

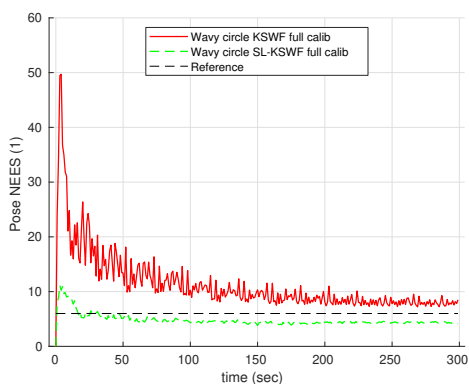


Fig. 5. Pose NEES for KSWF and SL-KSWF with full self-calibration on the artificial wavy circle data. Its reference value 6 is shown with a dashed line.

the latter, sensor parameters were further corrupted with noises in Table IV.

The simulation and estimation were repeated 100 times for an estimator. The pose RMSE values are reported in Table V. With inaccurate sensor parameters, both KSWF and SL-KSWF with full self-calibration achieved better or comparable accuracy to OKVIS, largely outperforming OKVIS that used inaccurate parameters. Moreover, NEES values [53] for these two methods shown in Fig. 5 indicate their consistency. Referring to Table V, calibrating mere IMU or camera parameters, the accuracy suffered much compared to full self-calibration. At the extreme of no calibration, these estimators diverged multiple times. These results indicate that full self-calibration benefits motion estimation when the prior calibration is inaccurate.

With the realistic corridor1 data, we reveal evolution of the estimated sensor parameters. The KSWF with full calibration were tested on this data using identical sensor and noise configurations to the wavy circle simulation. For a sample run, errors in the calibrated parameters and corresponding 3σ bounds over time are drawn in Fig. 6. All components decreased in uncertainty over time though at varying rates. The decreasing errors and tightening 3σ bounds validate that these parameters can be estimated reliably, corroborating analysis in

Section IV.

In summary, the simulation results show that KSWF can accurately estimate motion and fully calibrate the camera-IMU system with general motion.

VI. REAL-WORLD EXPERIMENTS

This section presents experiments on real data to validate advantages of keyframe-based filtering and full self-calibration. We report motion estimation with standstill periods first, and then motion estimation with full self-calibration. A previous evaluation of the SL-KSWF has been reported in [54].

To quantify estimation performance, pose accuracy was measured with Root Mean Square (RMS) of the Absolute Trajectory Error (ATE) consisting of rotational RMSE, and translational RMSE [55]. To compute the two metrics, the trajectory estimated by a VIO method was aligned to the ground truth with a transformation of a yaw-only rotation and a 3D translation.

In general, the compared methods were configured with as many default parameters as possible, and they processed data synchronously without enforcing real time execution unless this is not possible. To reduce randomness, results from five runs were used to compute the error metrics.

Throughout tests for KSWF, we used $N_{kf} = 5$ and $N_{tf} = 5$. A landmark was added to the state vector if it had been observed six times, and would be marginalized if it eluded three consecutive frame bundles. At maximum, 50 landmarks were kept in the state vector.

A. Motion Estimation with Standstills

We examined the drift issue of a monocular structureless filter in standstill by comparing several sliding window filters. The first four were KSWF, the non-keyframe version of KSWF (SWF) where every frame was taken as a keyframe and feature matching was only done between consecutive frames, and their structureless counterparts, SL-KSWF and SL-SWF, respectively. For the four filters, the self-calibration capability was turned off for clear comparison. Additionally, we also compared with ROVIO [12] which does not use a sliding window but keeps landmarks in the state vector and MSCKF-Mono [41] which uses frame-wise feature matching and keyframes in the backend filtering. In essence, the SL-SWF is very close to MSCKF-Mono since both are structureless and use frame-wise feature matching.

This test was conducted on the five Machine Hall sessions of the EuRoC benchmark [56] which have stationary periods. The datasets were captured indoors by a micro aerial vehicle (MAV) outfitted with GS stereo cameras and an industrial-grade IMU. This test used data captured by the IMU and the left camera for which the pinhole radial tangential model was used in the compared filters.

All filters initialized successfully and gave good motion estimates before a standstill. Then we could clearly see the effect of standstill on motion estimation. Fig. 7 visualizes the absolute velocity before and after standstills. The area under the velocity curve during standstill roughly represents the position drift. When the MAV landed, the frame-wise structureless

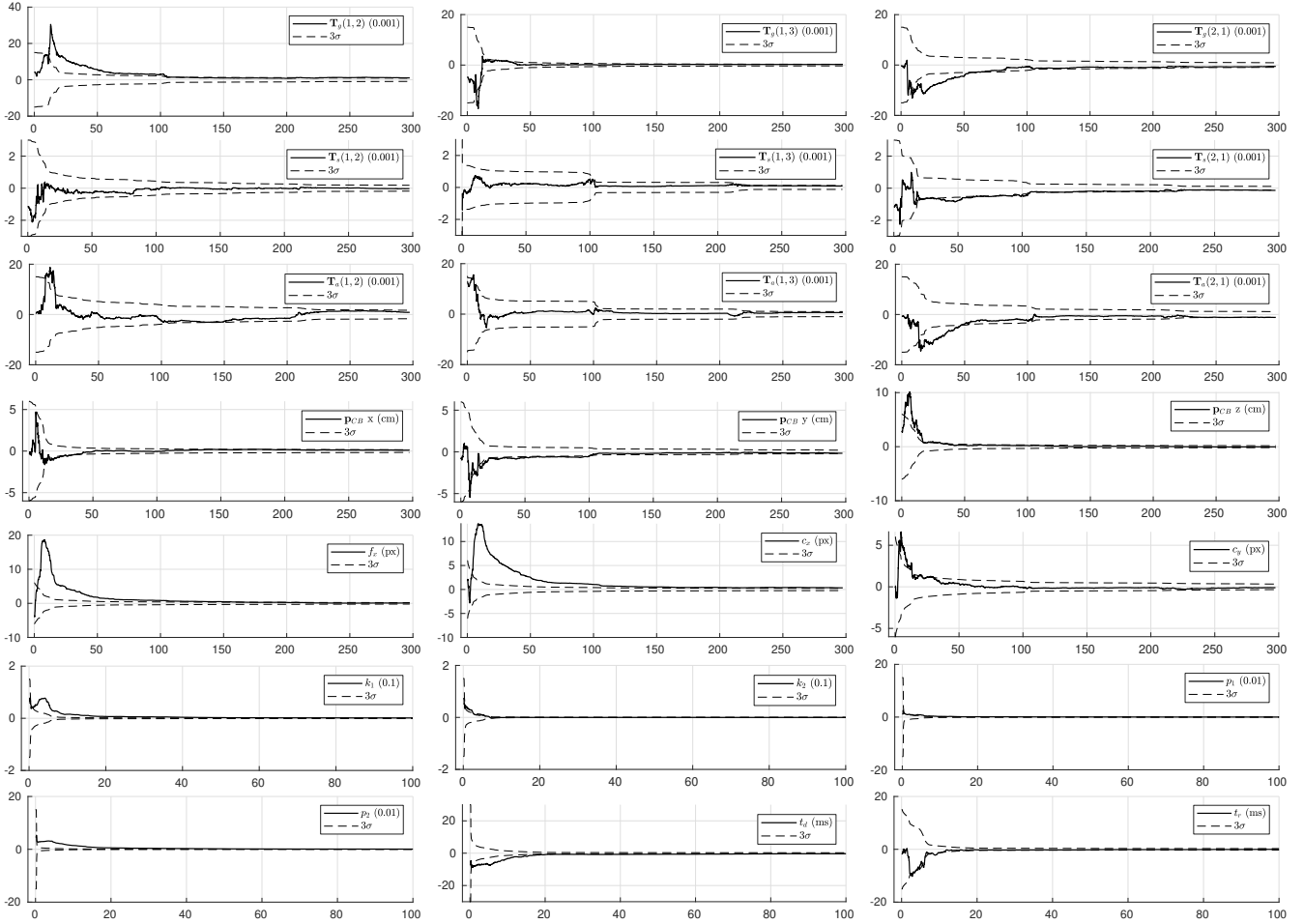


Fig. 6. Errors (solid lines) and 3σ bounds (dashed lines) of estimated camera-IMU system parameters in a sample run of KSWF on the data simulated from TUM VI corridor1 data. The x axis represents time in seconds. For brevity, only three off-diagonal elements of \mathbf{T}_g , \mathbf{T}_s , \mathbf{T}_a are shown.

filters, both MSCKF-Mono and SL-SWF, suffered position drifts, although MSCKF-Mono organizes state variables in terms of keyframes in the backend. Interestingly, both filters managed to estimate the velocity more or less accurately after the stationary periods. We think that the drift of MSCKF-Mono and SL-SWF is caused by frame-wise feature matching which provides many low disparity matches during standstills.

By contrast, filters that keep landmarks in the state, ROVIO, KSWF, and SWF, and filters that use keyframe-based matching, SL-KSWF and KSWF, reported almost zero velocity in standstill. On one hand, landmarks in the state vector serve as memory, constraining the filter during degenerate motion. On the other hand, feature matching relative to previous keyframes which do not depend on time retrieves matches of large disparity even during stationary periods.

This comparative test illustrates that keyframe-based feature matching helps structureless filters deal with degenerate motion, *e.g.*, standstill, and keeping landmarks in the state vector also resolves this issue.

B. Motion Estimation with Self-Calibration

To show the feasibility and benefits of self-calibration, tests were conducted on raw room sequences of the TUM

VI benchmark [51]. These sequences were captured by a handheld device with stereo GS cameras of fisheye lenses of diagonal FOV 195° and a consumer-grade IMU. Ground truth motion was recorded by a motion capture system, serving well to evaluate VIO methods. The authors have provided raw sequences, calibration data for the sensor setup, and calibrated sequences where the IMU data were corrected with the estimated IMU intrinsic parameters. For this test, we chose the six room sequences because they have diverse motion. The camera-IMU calibration results provided in the benchmark can serve as reference to validate the full self-calibration.

To prepare the raw sequences, images were down-scaled to 512×512 as in [51], and timestamps of camera and IMU messages were shifted by a constant duration to be aligned with the ground truth for the sake of evaluation.

Then, these sequences were processed by several recent VIO methods. Five KSWF variants were used including KSWF, SL-KSWF, KSWF without self-calibration, KSWF that calibrates only IMU intrinsics, and KSWF that calibrates only camera extrinsics, intrinsics, t_d^i , and t_r^i , $i = 0, 1$. For comparison, OKVIS [11] with extrinsic calibration, VINS-Mono [32] with extrinsic calibration, and OpenVINS [10] with camera intrinsic and spatiotemporal calibration were also used. Note that the

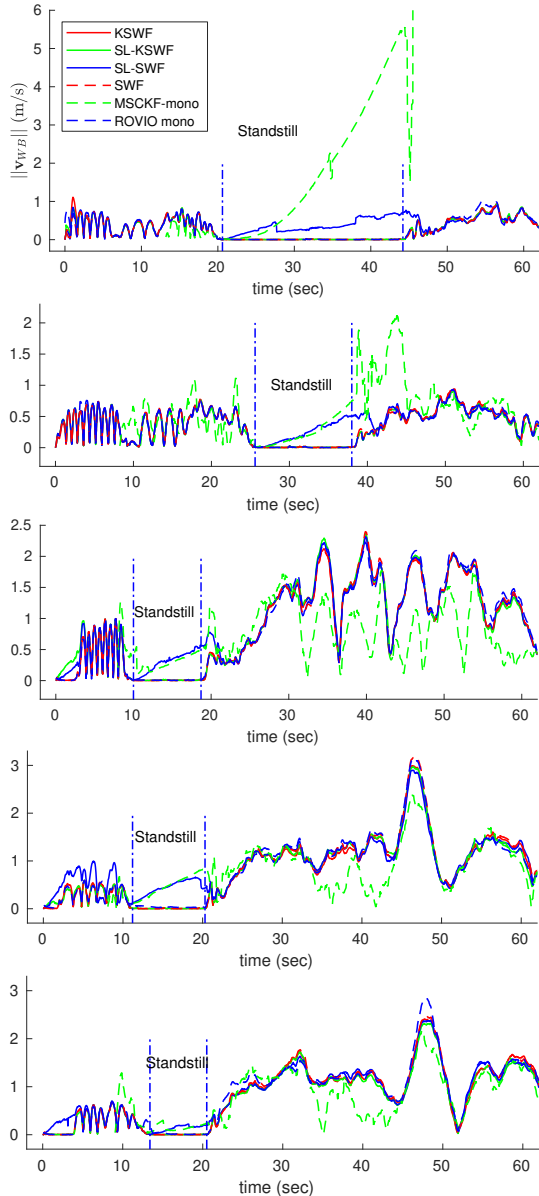


Fig. 7. Velocity estimated by KSWF, SL-KSWF, SWF, SL-SWF, MSCKF-mono, and ROVIO for EuRoC MH 1-5 sequences. All methods ran in monocular mode using the left camera images. SL-SWF and MSCKF-mono have nonzero velocity during standstills in contrast to other methods.

last variant of KSWF is similar to OpenVINS [10] in configuration. VINS-Mono only processed the left camera images and IMU data. Features of these methods are summarized in Table VI.

These methods were mostly configured using parameters provided by their authors, *e.g.*, OpenVINS and VINS-Mono. For OKVIS, the configuration file provided by the TUM VI benchmark was used as a starting point. Then, for all estimators, sensor parameters were initialized to nominal values. If a parameter was not to be calibrated, it was locked to the initial value. Initial values for IMU intrinsics are $\mathbf{T}_g = \mathbf{I}$, $\mathbf{T}_s = \mathbf{0}$, and $\mathbf{T}_a = \mathbf{I}$. The camera extrinsic parameters were set zero in translation and a nominal rotation in orientation. The Kannala Brandt 6-parameter model [47] were used for

TABLE VI
FEATURES OF THE COMPARED ODOMETRY METHODS.

Method	OKVIS	VINS-Mono	OpenVINS	KSWF
RS camera model		✓		✓
Calibrate cameras	Extrinsics	✓	✓	✓
	Intrinsics		✓	✓
	t_d	✓	✓	✓
	t_r			✓
Calibrate IMU	Intrinsics			✓
	Biases	✓	✓	✓

the stereo cameras with initial values $f_x^i = f_y^i = 190$ (px), $c_x^i = 256$ (px), $c_y^i = 256$ (px), $k_1^i = 0$, and $k_2^i = 0$ for $i = 0, 1$. The temporal parameters had initial values $t_d^i = 0$ s and $t_r^i = 0.02$ s for $i = 0, 1$. Because the raw sequences have large IMU errors, for all estimators, the IMU noise parameters were inflated from values provided by authors with a simple grid search.

For these estimators starting from inaccurate parameters, the error metrics of estimated motion versus the number of runs on the raw room sequences are drawn in Fig 8. Methods with very limited self-calibration, *e.g.*, OKVIS and VINS-Mono, suffered significantly in motion estimation accuracy and often diverged. This contrasts with their performance on the calibrated room sequences with accurate sensor parameters, for which all compared estimators estimated motion accurately without obvious drift, achieving $<0.2\%$ relative translation error [55]. Comparing the variants of KSWF, as the level of self-calibration increased, the motion estimation became less brittle and more accurate. This is particularly true when the IMU intrinsics were calibrated, likely because the consumer-grade IMU is notoriously affected by scale factor errors and misalignment. Interestingly, OpenVINS and KSWF that calibrated camera parameters had similar performance as both calibrated almost the same set of parameters.

To examine observability of parameters in full self-calibration, we compared their values estimated by KSWF and OpenVINS, and values provided by the benchmark. For reference, the benchmark's authors have estimated the IMU intrinsic and camera extrinsic parameters with their calibration data. For comparison, these values were converted to our notation. On the other hand, reference camera intrinsics were obtained with a program Basalt [57] using the calibration data. Besides the estimated parameters from the 27 convergent runs of KSWF in the previous test, we also calibrated camera-related parameters by running OpenVINS on the six calibrated room sequences. These estimated parameters with 3σ bounds and their references, relative to initial values, are visualized in Fig. 9. Since OpenVINS gives identical results for five runs on the same sequence, only one estimate of a parameter is drawn for each sequence.

For parameters estimated by KSWF, we see that: (1) \mathbf{b}_g , \mathbf{b}_a , \mathbf{T}_g , \mathbf{T}_s , t_d^i , t_r^i with $i = 0, 1$ were estimated consistently with small variances; (2) camera intrinsics f^i , c_x^i , c_y^i , k_1^i , $i = 0, 1$, and some dimensions of \mathbf{T}_a , had some estimates that

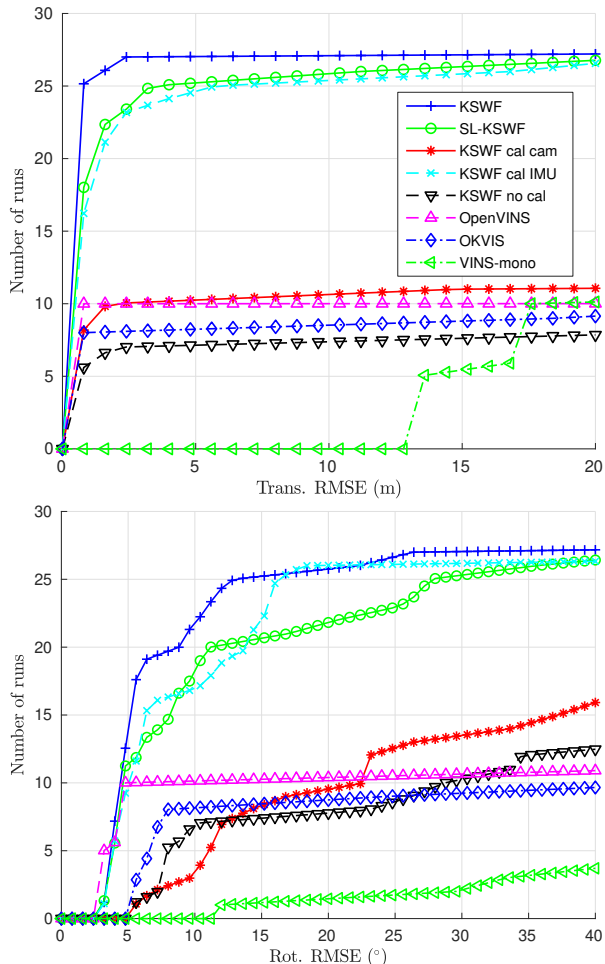


Fig. 8. Translation and rotation RMSE of odometry methods, KSWF with default full calibration, SL-KSWF with default full calibration, KSWF that calibrates only camera-related parameters, KSWF that calibrates only IMU parameters, KSWF without calibration, OKVIS, OpenVINS, VINS-mono, on the TUM VI six raw stereo room sequences. Each method ran five times on a sequence.

deviated much from the reference; and (3) the camera extrinsics \mathbf{p}_{C_0B} , \mathbf{p}_{BC_1} , and \mathbf{R}_{BC_1} had dispersed estimates in some components. Observations (2-3) indicate that some parameters of the camera-IMU system are more challenging to calibrate. Considering that all parameters were estimated mostly close to their references starting from the initial inaccurate values, this largely confirmed that these parameters are observable.

For OpenVINS, since the IMU intrinsic errors had been mostly corrected and only camera parameters were calibrated, we expect it to estimate parameters closer to the references and to have smaller variances than KSWF. Strangely, we see that k_2^i , $i = 0, 1$, had unusual large uncertainty, and some parameters consistently deviated from reference values, *e.g.*, k_1^0 , and $\mathbf{p}_{BC_1}(3)$.

To evaluate the efficiency of KSWF, we timed its three components, feature extraction, feature matching, and estimation including filter update and marginalization, with the EuRoC benchmark [56], on a Dell Inspiron 7590 laptop with 16 GB RAM and a 2.60 GHz 6-core Intel Core i7-9750H processor running Ubuntu 18.04. The time costs of components of SL-

TABLE VII
TIME COST OF MAJOR FUNCTIONS OF SL-KSWF IN PROCESSING EUROC SEQUENCES IN MILLISECONDS. VALUES IN **BOLD** INDENTIFY ROUTINES THAT DETERMINE AVERAGE TIME TO PROCESS A FRAME BUNDLE.

Function	Mono		Stereo	
	mean	σ	mean	σ
Feature extraction 0	3.0	0.3	5.1	1.5
Feature extraction 1	0	0	5.1	1.6
Match to keyframes	1.3	0.2	2.9	0.7
Match to last frame	0.7	0.1	1.8	0.5
Match left to right	0	0	0.5	0.1
Filter update	4.5	1.4	13.4	3.6
Marginalization	1.5	0.8	5.1	1.9
Time per frame	8.0	N/A	23.7	N/A

KSWF with full self-calibration and synchronous processing are presented in Table VII. The time costs of KSWF are slightly larger than SL-KSWF in filter update and marginalization, varying with the allowed number of landmarks in the state vector. As feature extraction is done in parallel, average processing time for a frame bundle amounts to the time costs for feature matching and estimation, thereby, 8 ms (125 Hz) in the monocular mode, and 23.7 ms (42.2 Hz) in the stereo mode, meaning that the proposed method has good efficiency.

VII. CONCLUSION AND FUTURE WORK

Regarding VIO with self-calibration, this paper solves two existing problems: whether the full set of calibration parameters are observable, and the drift issue in conventional structureless monocular filters under degenerate motion.

For the former, using Lie derivatives, we prove that camera intrinsics, extrinsics, time offset, and IMU intrinsics of the camera-IMU system are observable under general motion using observations of opportunistic landmarks. Given this condition, the frame readout time can be estimated. These observability assertions were confirmed with simulation and real data tests. We foresee that this type of symbolic computation can greatly simplify observability analysis of a slew of parameter estimation problems compared to manual derivation.

For the latter, we introduce the keyframe concept to both the feature matching frontend and sliding window filtering backend. Together with the self-calibration capability, this brings about the KSWF framework. Real world tests validated the strength of keyframe-based filtering, revealing that either keyframe-based matching or keeping landmarks in the state vector helps remedy the drift issue of structureless monocular filters in standstill. Moreover, on datasets captured by inaccurate sensors, KSWF with self-calibration largely outperformed recent VIO methods of minimal calibration, indicating the value of self-calibration for low-cost sensors.

Besides motion estimation, an interesting application of our method is to inspect the setup of legacy data. For example, by running KSWF on the TUM rolling shutter datasets [58], it is found that they were captured with the left camera in GS mode and the right camera in RS mode.

We are aware that full self-calibration will encounter unobservable dimensions when the camera-IMU system is confined in motion, *e.g.*, on a ground vehicle. In such situations, it is

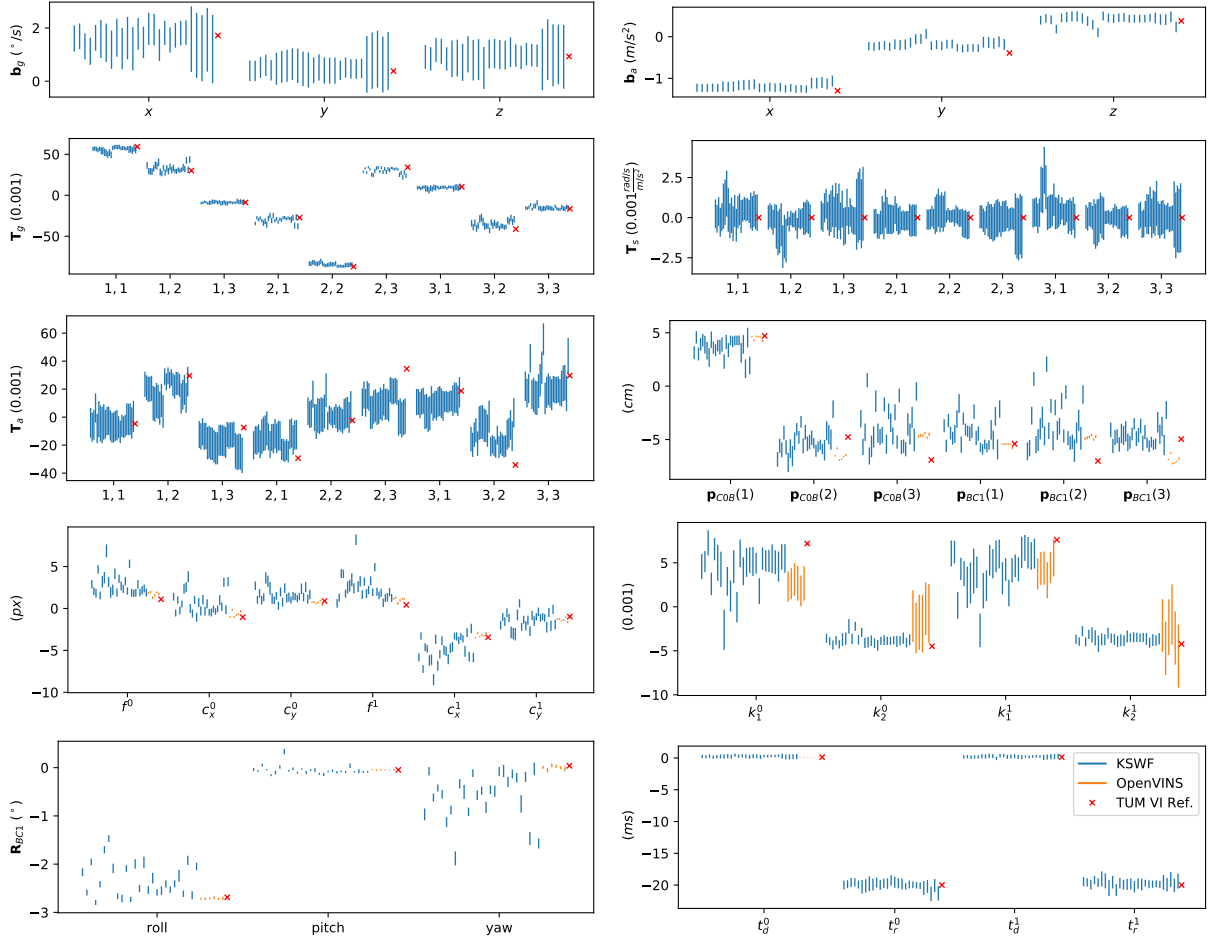


Fig. 9. Parameter estimates relative to initial values and 3σ bounds by KSWF on the six TUM VI raw room sequences and by OpenVINS on the six calibrated room sequences. Blue bars are for 27 successful runs of KSWF (five attempts for each sequence). Orange bars are for OpenVINS (one run for each sequence). Red crosses show reference values from the benchmark. Note that frame readout times were initialized to 20 ms.

advisable to lock up those unobservable parameters. To this end, identifying unobservable directions with Lie derivatives is one of the worthwhile directions to look into. A related problem is VIO initialization in the case of coarse calibration.

APPENDIX WHEN TIME OFFSET IS UNOBSERVABLE

This section identifies the condition when the time offset in outputs of an affine-input system is indistinguishable. For simple deduction, we rewrite the affine-input system (15) with scalar inputs u_i , $i = 1, 2, \dots, m$,

$$\dot{\mathbf{x}} = \mathbf{f}_0(\mathbf{x}) + \sum_{i=1}^m \mathbf{f}_i(\mathbf{x})u_i, \quad \mathbf{y} = \mathbf{h}(\mathbf{x}) \quad (31)$$

We try to find when $\mathbf{h}(\mathbf{x}(t+t_d)) = \mathbf{h}(\mathbf{x}(t))$ holds. The Taylor expansion for $\mathbf{h}(\mathbf{x}(t+t_d))$ regarding t_d is

$$\mathbf{h}(\mathbf{x}(t+t_d)) = \mathbf{h}(\mathbf{x}(t)) + t_d \dot{\mathbf{h}}(\mathbf{x}) + \frac{t_d^2}{2} \ddot{\mathbf{h}}(\mathbf{x}) + \frac{t_d^3}{6} \dddot{\mathbf{h}}(\mathbf{x}) + \dots \quad (32)$$

The first three derivatives are given by

$$\dot{\mathbf{h}}(\mathbf{x}(t)) = \nabla \mathbf{h} \cdot \dot{\mathbf{x}} = \mathcal{L}_{\mathbf{f}_0}^1 \mathbf{h} + \sum_{i=1}^m \mathcal{L}_{\mathbf{f}_i}^1 \mathbf{h} u_i \quad (33)$$

$$\begin{aligned} \ddot{\mathbf{h}}(\mathbf{x}) &= \nabla(\mathcal{L}_{\mathbf{f}_0}^1 \mathbf{h} + \sum_{i=1}^m \mathcal{L}_{\mathbf{f}_i}^1 \mathbf{h} u_i) \dot{\mathbf{x}} + \sum_{i=1}^m \mathcal{L}_{\mathbf{f}_i}^1 \mathbf{h} \dot{u}_i \\ &= \mathcal{L}_{\mathbf{f}_0, \mathbf{f}_0}^2 \mathbf{h} + \sum_{i=1}^m \mathcal{L}_{\mathbf{f}_0, \mathbf{f}_i}^2 \mathbf{h} u_i + \sum_{i=1}^m \mathcal{L}_{\mathbf{f}_i, \mathbf{f}_0}^2 \mathbf{h} u_i + \\ &\quad \sum_{j=1}^m \sum_{i=1}^m \mathcal{L}_{\mathbf{f}_i, \mathbf{f}_j}^2 \mathbf{h} u_i u_j + \sum_{i=1}^m \mathcal{L}_{\mathbf{f}_i}^1 \mathbf{h} \dot{u}_i \end{aligned} \quad (34)$$

$$\begin{aligned} \dddot{\mathbf{h}}(\mathbf{x}) &= \nabla(\mathcal{L}_{\mathbf{f}_0, \mathbf{f}_0}^2 \mathbf{h} + \sum_{i=1}^m \mathcal{L}_{\mathbf{f}_0, \mathbf{f}_i}^2 \mathbf{h} u_i + \sum_{i=1}^m \mathcal{L}_{\mathbf{f}_i, \mathbf{f}_0}^2 \mathbf{h} u_i + \\ &\quad \sum_{j=1}^m \sum_{i=1}^m \mathcal{L}_{\mathbf{f}_i, \mathbf{f}_j}^2 \mathbf{h} u_i u_j + \sum_{i=1}^m \mathcal{L}_{\mathbf{f}_i}^1 \mathbf{h} \dot{u}_i) \dot{\mathbf{x}} + \\ &\quad \sum_{i=1}^m \mathcal{L}_{\mathbf{f}_0, \mathbf{f}_i}^2 \mathbf{h} \dot{u}_i + \sum_{i=1}^m \mathcal{L}_{\mathbf{f}_i, \mathbf{f}_0}^2 \mathbf{h} \dot{u}_i + \sum_{i=1}^m \mathcal{L}_{\mathbf{f}_i}^1 \mathbf{h} \ddot{u}_i + \\ &\quad \sum_{j=1}^m \sum_{i=1}^m \mathcal{L}_{\mathbf{f}_i, \mathbf{f}_j}^2 \mathbf{h} \dot{u}_i u_j + \sum_{j=1}^m \sum_{i=1}^m \mathcal{L}_{\mathbf{f}_i, \mathbf{f}_j}^2 \mathbf{h} u_i \dot{u}_j \end{aligned} \quad (35)$$

The above expressions show that in general $\frac{d^k \mathbf{h}}{dt^k}$ is a linear combination of covectors (e.g., $\nabla \mathcal{L}_{\mathbf{f}_0, \mathbf{f}_i}^2$) with coefficients $\dot{\mathbf{x}}$, and time derivatives of inputs (e.g., $\mathcal{L}_{\mathbf{f}_i, \mathbf{f}_j}^2 \mathbf{h} \dot{u}_i u_j$). The condition to make t_d unobservable is that

$$\frac{d^k \mathbf{h}}{dt^k}(\mathbf{x}, u_i, \dot{u}_i, \dots) = \mathbf{0}, \quad k = 1, 2, \dots, \quad i = 1, 2, \dots, m \quad (36)$$

As with the observability analysis, we are free to choose u_i . By setting $u_i, i = 1, 2, \dots, m$, to constants in the time interval \mathcal{I} , (36) is satisfied when \mathbf{x} meets the below constraints,

$$\mathcal{O} \cdot \dot{\mathbf{x}} = \mathbf{0} \quad (37)$$

Otherwise, when $u_i, i = 1, 2, \dots, m$, are time varying and have non-vanishing time derivatives up to order k , there will be much fewer points in the space \mathcal{M} of \mathbf{x} satisfying (36). Intuitively, the reason is that under the set of constraints (36) on \mathbf{x} and $u_i, i = 1, 2, \dots, m$, the freedom of \mathbf{x} shrinks when the inputs u_i are allowed more freedom.

ACKNOWLEDGMENT

We would like to thank Agostino Martinelli for guidance on Lie derivatives. We are grateful to the Editor who awarded us four extensions. Moreover, we appreciate the inspiring comments from anonymous reviewers who exhorted us to novelty and contribution.

REFERENCES

- [1] A. Flint, O. Naroditsky, C. P. Broaddus, A. Grygorenko, S. Roumeliotis, and O. Bergig, "Visual-based inertial navigation," US Patent US9424647B2, Aug., 2016. 1, 2, 3
- [2] S. R. McClure, B. S. Thompson, A. Bry, A. Bachrach, and M. Donahoe, "Perimeter structure for unmanned aerial vehicle," US Patent US20170341776A1, Nov., 2017. 1
- [3] R. T. Pack, S. R. Lenser, J. H. Kearns, and O. Taka, "Simultaneous localization and mapping for a mobile robot," US Patent US9037396B2, May, 2015. 1
- [4] J. Huai, Y. Qin, F. Pang, and Z. Chen, "Segway DRIVE benchmark: Place recognition and SLAM data collected by a fleet of delivery robots," Segway Robotics, Beijing, China, Tech. Rep., Jul. 2019. 1
- [5] B. Bescos, C. Campos, J. D. Tardós, and J. Neira, "DynaSLAM II: Tightly-Coupled Multi-Object Tracking and SLAM," *IEEE Robotics and Automation Letters*, vol. 6, no. 3, pp. 5191–5198, Jul. 2021. 1
- [6] D. Zuñiga-Noël, F.-A. Moreno, and J. Gonzalez-Jimenez, "An analytical solution to the IMU initialization problem for visual-inertial systems," *arXiv:2103.03389 [cs]*, Mar. 2021. 1, 5
- [7] T. Schneider, M. Li, C. Cadena, J. Nieto, and R. Siegwart, "Observability-aware self-calibration of visual and inertial sensors for ego-motion estimation," *IEEE Sensors Journal*, vol. 19, no. 10, pp. 3846–3860, May 2019. 1
- [8] C. Guo, D. Kottas, R. DuToit, A. Ahmed, R. Li, and S. Roumeliotis, "Efficient visual-inertial navigation using a rolling-shutter camera with inaccurate timestamps," in *Robotics: Science and Systems (RSS)*, Berkeley, USA, Jul. 2014. 1, 3
- [9] M. Li, H. Yu, X. Zheng, and A. I. Mourikis, "High-fidelity sensor modeling and self-calibration in vision-aided inertial navigation," in *IEEE Intl. Conf. on Robotics and Automation (ICRA)*, Hong Kong, China, May 2014, pp. 409–416. 1, 2, 3, 5
- [10] P. Geneva, K. Eickenhoff, W. Lee, Y. Yang, and G. Huang, "OpenVINS: A research platform for visual-inertial estimation," in *Workshop on Visual-Inertial Navigation: Challenges and Applications at IROS*, Macau, China, Nov. 2019. 1, 3, 5, 6, 11, 12
- [11] S. Leutenegger, S. Lynen, M. Bosse, R. Siegwart, and P. Furgale, "Keyframe-based visual-inertial odometry using nonlinear optimization," *The International Journal of Robotics Research*, vol. 34, no. 3, pp. 314–334, Mar. 2015. 1, 2, 3, 5, 9, 11
- [12] M. Bloesch, M. Burri, S. Omari, M. Hutter, and R. Siegwart, "Iterated extended Kalman filter based visual-inertial odometry using direct photometric feedback," *The International Journal of Robotics Research*, vol. 36, no. 10, pp. 1053–1072, Sep. 2017. 1, 3, 6, 10
- [13] J. Kelly and G. S. Sukhatme, "Visual-inertial sensor fusion: Localization, mapping and sensor-to-sensor self-calibration," *The International Journal of Robotics Research*, vol. 30, no. 1, pp. 56–79, 2011. 1, 2
- [14] S.-H. Tsao and S.-S. Jan, "Observability analysis and performance evaluation of EKF-based visual-inertial odometry with online intrinsic camera parameter calibration," *IEEE Sensors Journal*, vol. 19, no. 7, pp. 2695–2703, Apr. 2019. 1, 2
- [15] J. H. Jung, S. Heo, and C. G. Park, "Observability analysis of IMU intrinsic parameters in stereo visual-inertial odometry," *IEEE Transactions on Instrumentation and Measurement*, vol. 69, no. 10, pp. 7530–7541, Oct. 2020. 1, 2
- [16] J. Huai, "Collaborative SLAM with crowdsourced data," Ph.D. dissertation, The Ohio State University, Columbus OH, May 2017. 1, 2, 4, 6
- [17] S. I. Roumeliotis and A. I. Mourikis, "Vision-aided inertial navigation," US Patent US9766074B2, Sep., 2017. 1
- [18] D. G. Kottas, K. J. Wu, and S. I. Roumeliotis, "Detecting and dealing with hovering maneuvers in vision-aided inertial navigation systems," in *2013 IEEE/RSJ International Conference on Intelligent Robots and Systems*. Tokyo: IEEE, Nov. 2013, pp. 3172–3179. 1
- [19] A. I. Mourikis and S. I. Roumeliotis, "A multi-state constraint Kalman filter for vision-aided inertial navigation," in *IEEE Intl. Conf. on Robotics and Automation (ICRA)*, Rome, Italy, Apr. 2007, pp. 3565–3572. 1, 2, 3, 6
- [20] J. A. Hesch, D. G. Kottas, S. L. Bowman, and S. I. Roumeliotis, "Camera-IMU-based localization: Observability analysis and consistency improvement," *The International Journal of Robotics Research*, vol. 33, no. 1, pp. 182–201, Jan. 2014. 1, 2, 3
- [21] M. Li and A. I. Mourikis, "High-precision, consistent EKF-based visual-inertial odometry," *The International Journal of Robotics Research*, vol. 32, no. 6, pp. 690–711, May 2013. 1, 3, 6
- [22] R. Hermann and A. Krener, "Nonlinear controllability and observability," *IEEE Transactions on Automatic Control*, vol. 22, no. 5, pp. 728–740, Oct. 1977. 2, 7
- [23] A. Martinelli, "Visual-inertial structure from motion: Observability and resolvability," in *2013 IEEE/RSJ International Conference on Intelligent Robots and Systems (IROS)*. Tokyo, Japan: IEEE, Nov. 2013, pp. 4235–4242. 2
- [24] K. Maes, M. N. Chatzis, and G. Lombaert, "Observability of nonlinear systems with unmeasured inputs," *Mechanical Systems and Signal Processing*, vol. 130, pp. 378–394, 2019. 2, 7
- [25] J. A. Hesch, D. G. Kottas, S. L. Bowman, and S. I. Roumeliotis, "Consistency analysis and improvement of vision-aided inertial navigation," *IEEE Transactions on Robotics*, vol. 30, no. 1, pp. 158–176, Feb. 2014. 2
- [26] Y. Yang, P. Geneva, K. Eickenhoff, and G. Huang, "Degenerate motion analysis for aided INS with online spatial and temporal sensor calibration," *IEEE Robotics and Automation Letters*, vol. 4, no. 2, pp. 2070–2077, Apr. 2019. 2, 8
- [27] F. M. Mirzaei and S. I. Roumeliotis, "A Kalman filter-based algorithm for IMU-camera calibration: Observability analysis and performance evaluation," *IEEE Transactions on Robotics*, vol. 24, no. 5, pp. 1143–1156, Oct. 2008. 2
- [28] A. Martinelli, *Observability: A new theory based on the group of invariance*, ser. Advances in Design and Control. Society for Industrial and Applied Mathematics, Jan. 2020. 2, 6, 7
- [29] —, "Vision and IMU data fusion: Closed-form solutions for attitude, speed, absolute scale, and bias determination," *IEEE Transactions on Robotics*, vol. 28, no. 1, pp. 44–60, Feb. 2012. 2
- [30] Y. Yang, P. Geneva, X. Zuo, and G. Huang, "Online IMU intrinsic calibration: Is it necessary?" in *Robotics: Science and Systems (RSS)*, Corvallis, Oregon, Jul. 2020, pp. 716–725. 2
- [31] M. Li and A. I. Mourikis, "Online temporal calibration for camera-IMU systems: Theory and algorithms," *The International Journal of Robotics Research*, vol. 33, no. 7, pp. 947–964, 2014. 2, 8
- [32] T. Qin, P. Li, and S. Shen, "VINS-Mono: A robust and versatile monocular visual-inertial state estimator," *IEEE Transactions on Robotics*, vol. 34, no. 4, pp. 1004–1020, Aug. 2018. 2, 3, 5, 11
- [33] V. Usenko, N. Demmel, D. Schubert, J. Stückler, and D. Cremers, "Visual-inertial mapping with non-linear factor recovery," *IEEE Robotics and Automation Letters*, vol. 5, no. 2, pp. 422–429, Apr. 2020. 2

- [34] D. Strelow and S. Singh, "Motion estimation from image and inertial measurements," *The International Journal of Robotics Research*, vol. 23, no. 12, pp. 1157–1195, Dec. 2004. 2
- [35] M. J. Veth, "Fusion of imaging and inertial sensors for navigation," Ph.D. dissertation, Airforce Institute of Technology, Dayton, OH, Sep. 2006. 2
- [36] E. S. Jones and S. Soatto, "Visual-inertial navigation, mapping and localization: A scalable real-time causal approach," *The International Journal of Robotics Research*, vol. 30, no. 4, pp. 407–430, Jan. 2011. 3
- [37] S. Weiss, M. W. Achtelik, S. Lynen, M. Chli, and R. Siegwart, "Real-time onboard visual-inertial state estimation and self-calibration of MAVs in unknown environments," in *IEEE Intl. Conf. on Robotics and Automation (ICRA)*, St Paul, MN, USA, May 2012, pp. 957–964. 3
- [38] K. Wu, A. Ahmed, G. Georgiou, and S. Roumeliotis, "A square root inverse filter for efficient vision-aided inertial navigation on mobile devices," in *Robotics: Science and Systems XI*. Robotics: Science and Systems Foundation, Jul. 2015. 3
- [39] K. Sun, K. Mohta, B. Pfrommer, M. Watterson, S. Liu, Y. Mulgaonkar, C. J. Taylor, and V. Kumar, "Robust stereo visual inertial odometry for fast autonomous flight," *IEEE Robotics and Automation Letters*, vol. 3, no. 2, pp. 965–972, Apr. 2018. 3, 6
- [40] G. Younes, D. Asmar, E. Shamma, and J. Zelek, "Keyframe-based monocular SLAM: Design, survey, and future directions," *Robotics and Autonomous Systems*, vol. 98, pp. 67–88, 2017. 3
- [41] A. Z. Zhu, N. Atanasov, and K. Daniilidis, "Event-based visual inertial odometry," in *2017 IEEE Conference on Computer Vision and Pattern Recognition (CVPR)*, Jul. 2017, pp. 5816–5824. 3, 10
- [42] D. Abeywardena, S. Huang, B. Barnes, G. Dissanayake, and S. Kodagoda, "Fast, on-board, model-aided visual-inertial odometry system for quadrotor micro aerial vehicles," in *2016 IEEE International Conference on Robotics and Automation (ICRA)*, May 2016, pp. 1530–1537. 3
- [43] C. Jekeli, *Inertial Navigation Systems with Geodetic Applications*. Berlin, Germany: de Gruyter, Jan. 2001. 4, 6
- [44] J. Huai, Y. Lin, Y. Zhuang, and M. Shi, "Consistent right-invariant fixed-lag smoother with application to visual inertial SLAM," in *35th AAAI Conference on Artificial Intelligence*, Feb. 2021. 4, 6
- [45] M. Li and A. I. Mourikis, "Vision-aided inertial navigation with rolling-shutter cameras," *The International Journal of Robotics Research*, vol. 33, no. 11, pp. 1490–1507, 2014. 4, 5, 6
- [46] G. R. Bradski and A. Kaehler, *Learning OpenCV: Computer vision with the OpenCV library*, 1st ed. Sebastopol, CA, USA: O'Reilly Media, Inc., 2008. 4
- [47] J. Kannala and S. S. Brandt, "A generic camera model and calibration method for conventional, wide-angle, and fish-eye lenses," *IEEE Transactions on Pattern Analysis and Machine Intelligence*, vol. 28, no. 8, pp. 1335–1340, Aug. 2006. 4, 8, 12
- [48] S. Leutenegger, M. Chli, and R. Y. Siegwart, "BRISK: Binary robust invariant scalable keypoints," in *Intl. Conf. on Computer Vision (ICCV)*, Barcelona, Spain, Nov. 2011, pp. 2548–2555. 5
- [49] F. Devernay and O. Faugeras, "Straight lines have to be straight," *Machine Vision and Applications*, vol. 13, no. 1, pp. 14–24, Aug. 2001. 8
- [50] B. Khomutenko, G. Garcia, and P. Martinet, "An enhanced unified camera model," *IEEE Robotics and Automation Letters*, vol. 1, no. 1, pp. 137–144, Jan. 2016. 8
- [51] D. Schubert, T. Goll, N. Demmel, V. Usenko, J. Stückler, and D. Cremers, "The TUM VI benchmark for evaluating visual-inertial odometry," in *IEEE/RSJ Intl. Conf. on Intelligent Robots and Systems (IROS)*, Madrid, Spain, Oct. 2018. 9, 11
- [52] T. Schneider, M. Dymczyk, M. Fehr, K. Egger, S. Lynen, I. Gilitschenski, and R. Siegwart, "Maplab: An open framework for research in visual-inertial mapping and localization," *IEEE Robotics and Automation Letters*, vol. 3, no. 3, pp. 1418–1425, 2018. 9
- [53] Y. Bar-Shalom, X. Li, and T. Kirubarajan, *Estimation with applications to tracking and navigation: Theory algorithms and software*. John Wiley & Sons, 2004. 10
- [54] J. Huai, Y. Lin, C. Toth, Y. Zhuang, and D. Chen, "A versatile keyframe-based structureless filter for visual inertial odometry," Wuhan University, Hubei, China, Tech. Rep., Dec. 2020. 10
- [55] Z. Zhang and D. Scaramuzza, "A tutorial on quantitative trajectory evaluation for visual(-inertial) odometry," in *IEEE/RSJ Intl. Conf. on Intelligent Robots and Systems (IROS)*, Madrid, Spain, Oct. 2018, pp. 7244–7251. 10, 12
- [56] M. Burri, J. Nikolic, P. Gohl, T. Schneider, J. Rehder, S. Omari, M. W. Achtelik, and R. Siegwart, "The EuRoC micro aerial vehicle datasets," *The International Journal of Robotics Research*, vol. 35, no. 10, pp. 1157–1163, 2016. 10, 13
- [57] V. Usenko, N. Demmel, and D. Cremers, "The double sphere camera model," in *2018 International Conference on 3D Vision (3DV)*. Verona, Italy: IEEE, Sep. 2018, pp. 552–560. 12
- [58] D. Schubert, N. Demmel, L. von Stumberg, V. Usenko, and D. Cremers, "Rolling-shutter modelling for direct visual-inertial odometry," Technical University of Munich, Germany, Tech. Rep., Nov. 2019. 13